

Single Charge-Exchange In Ion-Ion Collisions

by

Chun-Yen Chen

B.S., National Taiwan Normal University, 1988

A DISSERTATION

Submitted in partial fulfillment of the
requirements for the degree

DOCTOR OF PHILOSOPHY

Department of Physics
College of Art and Science

KANSAS STATE UNIVERSITY
Manhattan, Kansas

1998

Approved by:

Abstract

In order to study ion-ion collisions, a crossed-beam system has been implemented and tested in the J. R. Macdonald laboratory at Kansas State University. Ions coming from an ECR ion source intersect at 90 degrees with other ions coming from either a Penning ion source or from the KSU CRYEBIS (Kansas State University Cryogenic Electron Beam Ion Source). We have tested our system by measuring the total cross sections of single charge-exchange in ($He^{2+} - He^+$) at center-of-mass energies ranging from 1.775 to 14.775 keV. Our results are in very good agreement with the data measured by the Giesen group which demonstrates our ion-ion collision system is working properly. In addition to the $He^{2+} - He^+$ collision system, we have also measured the total cross sections of single charge-exchange in $Ne^{2+} - Ne^+$ and $Ar^{2+} - Ar^+$ collisions which have not been studied before. From our measurements the cross sections of $Ne^{2+} - Ne^+$ are about 1.3 times larger than those of $He^{2+} - He^+$, and those of $Ar^{2+} - Ar^+$ are about 2.7 times larger than those of $He^{2+} - He^+$. Theoretical calculations for $Ne^{2+} - Ne^+$ and $Ar^{2+} - Ar^+$ collisions have been carried out by E. Sidky and I. Reiser by using a one-electron potential model code. The predictions from these calculations are in very good agreement with our measurements.

Table of Contents

List of Figures	viii
Acknowledgements	ix
Acknowledgements	xi
1 Introduction	1
1.1 Motivation	1
1.2 Experimental difficulties	3
1.3 Survey of the previous work	3
1.3.1 Protons on singly charged ions	4
1.3.2 Singly charged ion pairs	5
1.3.3 H^- on multiply charged ions	5
1.3.4 Singly on multiply and multiply on multiply charged ions	6
1.3.5 Angular differential cross sections	10
2 General Setup	11
2.1 Experimental approaches	11

2.2	Overview	12
2.3	Before collisions	14
2.3.1	ECR beam line	14
2.3.2	EBIS beam line	18
2.4	Collision region	19
2.4.1	Decel-Accel columns	20
2.4.2	Central slit	20
2.5	After collision	22
2.5.1	ECR beam line	23
2.5.2	EBIS beam Line	24
3	Electronics Scheme	26
4	Data-Analysis	29
4.1	Data analysis	29
4.2	Results and discussions	39
4.2.1	Single charge-exchange in $He^{2+} - He^+$ collisions	39
4.2.2	Single charge-exchange in $Ne^{2+} - Ne^+$ and $Ar^{2+} - Ar^+$ collisions	43
5	Concluding Remarks	53
	Appendix	55
A	Beam Optics Calculations	55

B Lifetime Of He⁺ Metastable States	73
C Detector Efficiency Measurements	75
C.1 General theory	75
C.2 Setup	78
C.3 Results and discussions	79
Bibliography	85

List of Figures

2.1	A schematic drawing of the KSU ion-ion collision facility	13
2.2	The beam-optic elements in the collision system	17
2.3	The design of the central slit	21
3.1	Electronics setup for the ion-ion collision experiments	28
4.1	ECRXY: 2-D image of the ECR detector; EBISXY: 2-D image of the EBIS detector; ALLTAC: all of the time coincidences; GTAC: gated time coincidences.	31
4.2	The true ion-ion collision signals on the ECR detector (background subtracted); ECRX1: signals on detector X-position; ECRY1: signals on detector Y-position.	32
4.3	The true ion-ion collision signals on the EBIS detector (background subtracted); EBISX1: signals on detector X-position; EBISY1: signals on detector Y-position	33
4.4	Form factor measurement: linear current density vs central slit position	37

4.5	The energy dependence of the total cross sections of single charge exchange in $He^{2+} - He^+$ collisions [49].	39
4.6	The energy dependence of the total cross sections of single charge-exchange in $He^{2+} - He^+$ collisions	41
4.7	The energy dependence of the total cross sections of single charge-exchange in $Ne^{2+} - Ne^+$ collisions	45
4.8	The energy dependence of the total cross sections of single charge-exchange in $Ar^{2+} - Ar^+$ collisions	46
4.9	The energy dependence of the total cross sections of single charge-exchange in $Ar^{2+} - Ar^+$, $Ne^{2+} - Ne^+$ and $He^{2+} - He^+$ collisions. . .	47
4.10	The energy level diagrams for single charge-exchange in $Ne^{2+} - Ne^+$ and $Ar^{2+} - Ar^+$ collisions	52
A.1	3-D plot of the ECR beam line: including the EQ1, the deceleration column and the collision region.	56
A.2	A voltage contour plot of the ECR pre-collision region: $V_{retarding}=4$ kV; $V = \pm 95$ volts on quadrupole 1 and 3 ; $V = \pm 104$ volts on quadrupole 2.	57
A.3	Horizontal(X): ECR primary beam He^{2+} starts from the 2nd set of 4-jaw slits (bottom): He^{2+} : 10 keV, full width=3 mm, half angle= 0.2° , time marker: 50 nsec. The beam size at the center of the collision region is about 5.3 mm.	58

A.4	Vertical(Y): ECR primary beam He^{2+} starts from the 2nd set of 4-jaw slits (bottom): He^{2+} : 10 keV, full width = 4 mm, half angle= 1^0 , time marker: 50 nsec. The beam size at the center of the collision region is about 3.0 mm.	59
A.5	A voltage contour plot of the ECR post-collision region: $V_{retarding}=4$ kV, einzel lens:(-4.9 kV).	60
A.6	Horizontal(X):ECR charge-exchange beam He^+ starts from the center of the collision region (top): He^+ :2 keV, full width=5.3 mm, half angle= (-0.2408^0) , time marker:50 nsec. The beam size at the bottom of the plot (F-cup position) is about 6.7 mm.	61
A.7	Vertical(Y):ECR charge-exchange beam He^+ starts from the center of the collision region (top): He^+ :2 keV, full width=3 mm, half angle= (-0.84^0) , time marker:50 nsec. The beam size at the bottom of the plot(F-cup position) is about 11.4 mm.	62
A.8	A voltage contour plot of the ECR 45^0 electrostatic deflector: $V=(\pm 1.5kV)$ on the plates.	63
A.9	Horizontal(X) : ECR charge-exchange beam He^+ starts from the F-cup (top) : He^+ : 6 keV, full width= 6.7 mm, half angle = (0.1104^0) , time marker : 50 nsec. The beam size at the detector position is about 8.8 mm.	64

A.10 Vertical(Y) : ECR charge-exchange beam He^+ starts from the F-cup (top) : He^+ : 6 keV, full width = 11.4 mm, half angle = (-0.15^0) , time marker : 50 nsec.	65
A.11 A voltage contour plot of the EBIS prior-collision region : $V_{retarding} = 4$ kV.	66
A.12 EBIS Primary beam He^+ :trajectories are traced back from the center of the collision region(bottom) to the 4-jaw slit: He^+ :1.55 keV, full width=4 mm, half angle= (1.05^0) , time marker: 50 nsec. The beam size at the end of the plot(4-jaw slit) is about 4.5 mm.	67
A.13 A voltage contour plot of the EBIS post-collision region: $V_{retarding}=4$ kV; einzel lens: (-2.9) kV.	68
A.14 EBIS charge-exchange beam He^{2+} starts from the center of the collision region (top) to the downstream F-cup: He^{2+} :1.55 keV, full width=4 mm, half angle= (-1.05^0) , time marker: 50 nsec. The beam size at the F-cup (bottom) is about 6.9 mm.	69
A.15 A voltage contour plot of the EBIS 20^0 electrostatic deflector: $V=$ $(\pm 0.32kV)$ on the plates.	70
A.16 Horizontal(X):EBIS charge-exchange beam He^{2+} starts from the F- cup (top): He^{2+} :9.55 keV, full width=7.0 mm, half angle= (0^0) , time marker:50 nsec. The beam size at the detector position is about 7.0 mm.	71

A.17 Vertical(Y):EBIS charge-exchange beam He^{2+} starts from the F-cup (top): He^{2+} :9.55 keV, width=7.0 mm, half angle= (0^0) , time marker:50 nsec.	72
C.1 The gas pressure dependence of the capture count rate	82
C.2 The gas pressure dependence of the capture current	83
C.3 The energy dependence of the detector detection efficiency	84

Acknowledgements

There are so many people that I would like to thank, but I can only list some of them here.

First, I would like to express my great appreciation to Prof. Martin Stockli, my major advisor, for his guidance in research, for his understanding and encouragement when the time was difficult. I would also like to thank my committee members: Prof. Chii-Dong Lin and Prof. Brett DePaola for their guidance, and for their Thanksgiving dinners. Prof. Pat Richard for his generous financial support to attend conferences. Special thanks go to my outside committee member Prof. James Edgar and committee chairperson Prof. Chi Lung Huang for serving on my committee.

I would like to give my tremendous appreciation to Prof. C. Lewis Cocke for helping find our first ion-ion collision TAC peak (Nov. 20, 1995), and for his guidance in my research even though he is not my committee member. My appreciation also goes to Prof. F. Melchert, at Justus Liebig University, Giessen, Germany, for both helping design the ion-ion collision system and being a great mentor in ion-ion collision research.

I would also like to thank Dr. Emil Sidky and Ingrid Reiser for providing one-electron potential model calculations to make this dissertation more interesting. Special thanks go to Allen Landers and again, Ingrid Reiser, for proof-read this dissertation, and for their great help in setting up and running ion-ion collision experiments; Thanks also go to Dr. Mohammad Abdallah, Bernhard Walch, Suzanne Maleki, Peter Nelson and Eric Wells for their friendship, and for generously providing help whenever it was needed.

I give my respects to the members of the excellent JRM support staff especially Dr. Kevin Carnes and Vince Needham for their excellent computer support, Paul Gibson for his expertise and friendship; Bob Geering and Dave Hill for all the great machine work they did for this new collision system.

At this moment I would like to express my deep gratitude to my husband, Yi-Wei, for his love, support and sacrifice. I am grateful for the love and support of my parents and my siblings. My gratitude also goes to Yi-Wei's parents and siblings for their support and encouragement.

I wish to acknowledge the financial support from the Division of Chemical Sciences, Office of Basic Energy Sciences, Office of Energy Research, U.S. Department of Energy.

Acknowledgements

*In memory of
Dr. John P. Giese*

Chapter 1

Introduction

1.1 Motivation

Collisions between two charged particles (ion-ion) is a fundamental process inside plasmas. An ion can change its charge state via collisions with another ion. A detailed knowledge of ion-ion collisions will help our understanding of the charge state evolution and ion density distribution inside plasmas. However, to date the physics of ion-ion collisions has not been explored very thorough either experimentally or theoretically.

The first experimental study of ion-ion collisions between two positively charged ions was first reported in the 1960's; more reliable experimental data became available in 1970's [1–4]. Since then, the study of ion-ion collisions has concentrated on some particular systems which are directly related to the fusion research. Most of the experiments carried out to date have studied the collisions between two singly charged

ions. For simple collision systems like $(H^+ - He^+)$ and $(He^+ - He^+)$, theories based on close-coupling calculations have been very successful in describing the capture process over the entire range of collision energies [1]. At low collision energies, where the relative collision velocity is smaller than the orbital velocity of the valence electron, capture dominates ionization. One distinct phenomenon in the energy dependence of the resonant capture cross section in ion-ion collisions is the energy threshold below which the capture cross section drops quickly. This is due to Coulomb repulsion between the positive nuclei. As the collision energy increases to where the relative collision velocity is not much different from the orbital velocity of the valence electron, capture and ionization are competing processes. The cross sections for ionization have been measured and calculated and are in poor agreement with each other. Ionization in the intermediate collision energy range has not been understood as well as capture in the simple collision systems [1].

However, ion-ion collisions between two multiply charged ions have remained almost untouched with experiments far behind theory. Based on successes in ion-atom collisions, theorists have been trying to find general rules to describe charge-exchange in ion-ion collisions but calculations published by different groups using different approaches to describe the same collision system do not agree with each other [5]. Also, there is no experiment to verify the calculations.

Therefore, a more consistent experimental study is needed to improve our understanding of ion-ion collisions.

1.2 Experimental difficulties

The major difficulty in performing an ion-ion collision experiment is the thin target density from an ion beam. The intensity of an ion beam is limited naturally by space charge and will always be reduced artificially by system slits and apertures controlling the divergence of an ion beam. Usually, the effective target density presented by an ion beam ($\approx 10^6 \text{ cm}^{-3}$ or less) is many orders of magnitude smaller than a gas target ($\approx 10^{10} \text{ cm}^{-3}$ or more), and is comparable to the residual gas in an ultra high vacuum (10^{-10} torr) system ($\approx 10^6 \text{ cm}^{-3}$). The experimental difficulties caused by the thin target density are low signal count rate and poor signal to background ratio. (Sometimes signals are completely masked by backgrounds). Techniques like beam-pulsing and time-coincidence have been used by experimental groups to extract signals from the background.

1.3 Survey of the previous work

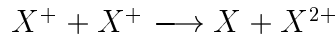
Progress in ion-ion collisions had been reviewed by E. Salzborn [1], K. F. Dunn [2], K. Dolder and B. Peart [3, 6], and H.B. Gilbody [4]. In addition to measuring total cross sections for capture using two singly charged ion beams [1, 7–26], a few experimental groups also carried out measurements involving multiply charged ion beams [27–29]. The measurements of the angular differential cross sections of charge exchange in ion-ion collisions were reported recently [28, 30, 31].

1.3.2 Singly charged ion pairs

Many experiments have been carried out to measure the total yield of doubly charged ions [1,17–26], that is



Separate measurements for capture



are only available for the $X=\text{He}$, Xe , Cs , and Bi systems. The simplest collision system among all these is $\text{He}^+ - \text{He}^+$ as it involves only two electrons in the collision. The difficulty for theorists in modeling the collision processes increases with the number of electrons. At low collision energies ($E_{cm} \leq 100$ keV), capture cross sections measured by experiments are in good agreement with theoretical calculations [37–39]. Theories indicate that capture into the spin-triplet states is the dominant channel. When the collision energy exceeds 100 keV, there are discrepancies in experimental data measured by different groups [17]. For ionization, the measurements from different groups are in good agreement with each other. However, only a few calculations [39, 40] are available, and the predictions from them are not in good accord with experiments [1].

1.3.3 H^- on multiply charged ions



The neutralization of H^- in energetic collisions with multiply charged ions has been studied both experimentally and theoretically by Melchert *et al* [41]. Quantum calculations were carried out to describe the behavior of neutralization and good agreement between their calculations and measurements was achieved. Based on their results, the neutralization cross sections in the above collision systems are independent of the target ion species, and a scaling rule was found between the scaled cross sections (σ/q) and the scaled collision energies (E_{cm}/q).

1.3.4 Singly on multiply and multiply on multiply charged ions

This area has remained virtually untouched on the experimental side except for the resonant single charge-exchange in the collision system



The energy dependence of these total cross sections has been heavily studied both theoretically [5,42–46] and experimentally [47–50]. The experimental difficulty in this collision system is the angular scattering of the reaction products. The colliding ions repel each other before and after the collision. The small cross sections measured by Jognaux *et al* [47] and Peart *et al* [48] at low collision energies were the results of insufficient angular acceptance for the reaction products [49]. Recently the measurements carried out by Melchert *et al* [50] at intermediate collision energies are in very good agreement with theoretical calculations. In order to test our new system,

we have also performed measurements at energies, some of which overlap those of Melchert *et al*, and good agreement with their measurements has been achieved.

Collisions between two multiply charged ions were first studied theoretically [51, 52]. Janev and Belic calculated the total cross sections of quasi-resonant single charge exchange in ion-ion collisions based on a two-state Rosen-Zener-Demkov model [51]. The calculations show that the cross sections are big, having an order of magnitude of 10^{-16} cm², and have very strong oscillations at high collision energies. Janev and Belic also employed the impact parameter method to study the cross sections of resonant double charge exchange in ion-ion collisions [52]. Besides these calculations, T. G. Winter [53] has used the coupled-Sturmian-pseudostate approach to calculate the cross sections of capture and ionization in collisions between protons and hydrogenic ions. His calculations show that the scaled total cross sections, $Z^7 \cdot \sigma^c(z)$, of capture fall closely on a universal curve when plotted as a function of the scaled relative collision energies, $E/(25Z^2)$. The same effect is found on the scaled ionization cross sections, $Z^4 \cdot \sigma^i(z)$, where Z is the atomic number of the hydrogenic ion. Later, Bardsley *et al* [46] and Tharamel *et al* [5] have independently investigated the cross sections of single charge transfer in some symmetric ion-ion collision systems. They both applied the impact parameter method but with different approaches for the energy difference in the transition probability calculation. They both calculated the cross sections for the $(Li - Li^+)$ -like collision series from $(Be^+ - Be^{2+})$ up to $(O^{5+} - O^{6+})$. Their results are quite different not only in the magnitude but also in the shape. The cross sections from Tharamel *et al* are about a factor of two

higher than those from Bardsley *et al* and contain oscillation structures. According to Tharamel *et al* the cross sections for charge exchange in symmetric ion-ion collisions may be generated from their isoelectronic ion-atom collisions by following a general formula. However, there is no experiment to verify these calculations.

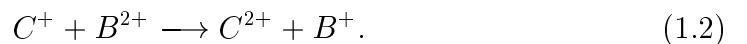
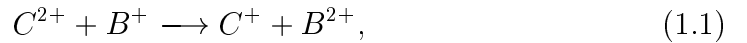
The first experimental approach to study ion-ion collisions with two multiply charged ion beams was reported by Kim and Janev [27]. They measured the cross sections of electron-loss in symmetric collisions,



at $E_{cm} = 60$ keV by using a folded-beam ion-ion collider. But, no detailed theoretical calculations were available for comparison.

Recently, experiments involving collisions of a singly or multiply charged ion beam with another multiply charged ion beam have been reported by the group in Justus Liebig University, Giessen, Germany. The following systems have been reported by them:

- (A)quasi-resonant single charge exchange



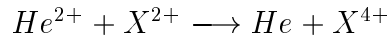
Brandau *et al* [54,55] measured the cross sections of reaction (1.1) and compared the results with the calculations by Janev and Belic [51]. The measured cross sections were found to deviate from the predictions of the calculations, both in shape and magnitude.

- (B) single charge exchange

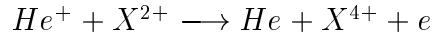


The total cross sections have been measured by Meuser *et al.* [28] Their results are very new and no calculations have been reported so far for comparison.

- (C) double charge exchange— two-electron process



- (D) transfer ionization— two-electron process



The cross sections for collisions in (C) and (D) have been measured by Melchert *et al* [29] for X=Ne, Ar, Kr and Xe at (0.6×10^6 m/sec $\leq v_{relative} \leq 5 \times 10^6$ m/sec) and (0.5×10^6 m/sec $\leq v_{relative} \leq 3 \times 10^6$ m/sec), respectively. These are also only experimental measurements without any theoretical calculations for comparison. experimental measurements without any theoretical calculations for comparison. experimental measurements without any theoretical calculations for comparison. experimental measurements without any theoretical calculations for comparison.

experimental measurements without any theoretical calculations for comparison. experimental measurements without any theoretical calculations for comparison.

1.3.5 Angular differential cross sections

Angular differential cross sections are more sensitive to theoretical models than total cross sections. However, experimental studies of angular differential cross sections in ion-ion collisions are scarce. Calculations of the impact parameter dependence of electron capture in $(H^+ - He^+)$ and $(He^+ - He^{2+})$ have been reported by some groups [32–34,44,45]. In recent years the pioneering group in Justus Liebig University, Giessen, Germany began publishing some measurements. Pfeiffer *et al* [30] measured angular scattering for the collision systems: $(H^+ - He^+)$ and $(He^+ - He^+)$. They claimed that their results should be treated as preliminary because the absolute primary beam density profile in two dimensions was not well defined. Krudener *et al* [31] reported measurements for the $(He^{2+} - He^+)$ collision system at $E_{cm} = 0.5$ keV and 10.2 keV. They observed oscillations in the differential cross sections and interpreted these to be the interference between *gerade* and *ungerade* electronic states of the ionic molecule. However, theory and measurement are only in fair agreement. Collisions between $He^{2+} - C^{3+}$ have also been measured by Meuser *et al* [28] but with no theories to compare with.

Chapter 2

General Setup

2.1 Experimental approaches

A detailed description of various experimental approaches to measure the absolute total cross sections in beam-beam interactions was given by Brouillard and Claeys in 1983 [56]. The experimental techniques employed in ion-ion collisions can be categorized into two types: merged-beam ($\theta = 0$) and crossed-beam ($\theta \neq 0$) methods, each having its own advantages [3]. For example, the merged-beam method provides access to very low collision energies even when working with very energetic beams. It usually offers a longer effective interaction length which is very helpful for experiments with very low target density, especially for ion-ion collision experiments. However, the disadvantage is that the overlap of the ion beams are not easy to determined. As to the crossed-beam method, the interaction geometry is better defined, and the spatial overlap of two beams is easier to measure. The spatial overlap is related to

the determination of the absolute cross sections in ion-ion collisions. The crossed-beam method, therefore, provides a more reliable way to measure the absolute cross sections.

2.2 Overview

Fig. 2.1 shows a schematic drawing of the new 90 degree crossed-beam ion-ion collision system. Ions from a 5 GHz ECR ion source intersect at 90 degrees with ions from either a Penning ion source or the KSU CRYEBIS. This ECR ion source can produce high intensity, moderate-charge ions with energies up to $(10 \times Q)$ keV where Q is the ion charge. The Penning ion source can produce high intensity but singly charged ions with energies (< 10 keV). The KSU CRYEBIS can produce very highly charged but low intensity ions with a broad energy range between $(0.3 \times Q)$ keV to $(165 \times Q)$ keV. With the combinations of ECR-Penning and ECR-EBIS, this new system will allow us to study ion-ion collisions with ions having a variety of charge states over a wide range of collision energies. Our measurements of the total cross sections of single charge exchange in $(He^{2+} - He^+)$, $(Ne^{2+} - Ne^+)$ and $(Ar^{2+} - Ar^+)$ were carried out under the ECR-Penning mode. In general, ions coming out of a source are momentum analyzed by an analyzing magnet, and then decelerated in the collision region. The overlap of ion beams in the collision region are scanned in vertical direction by a horizontal single slit oriented 45 degrees with respect to each ion beam. After collisions, the primary ions and charge-changed ions are separated downstream by an analyzing magnet. The primary ions are collected in a Faraday cup. The current is digitized

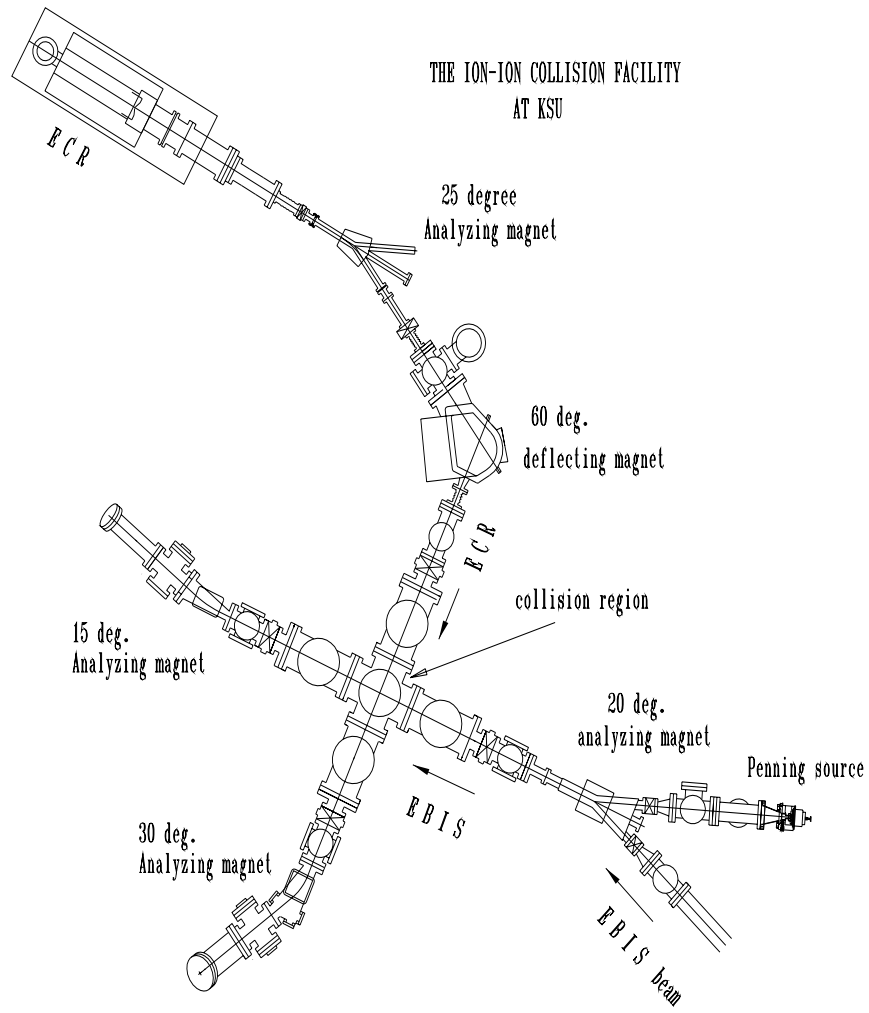


Figure 2.1: A schematic drawing of the KSU ion-ion collision facility

by a current integrator and recorded on a computer. The charge-changed ions keep traveling downstream and are further analyzed by an electrostatic analyzer. Finally, they are detected on a position-sensitive backgammon-anode detector at the end of the beam-line.

2.3 Before collisions

2.3.1 ECR beam line

Source The ion source installed in this beam line is a 5 GHz ECR (electron cyclotron resonance) ion source. This single stage ECR ion source was built at the Justus Liebig University, Giessen, Germany. Detailed descriptions of the ion source have been published [57, 58]. Generally speaking, the mechanism for producing positive-charge ions inside an ECR ion source is electron impact ionization. In order to create highly charged ions, two conditions must be met. First, the target ion has to be impacted by energetic electrons many times, because usually only one electron will be removed from a target ion in a single collision. Second, the impact electrons need to be energetic, because the binding energies of target electrons are higher for inner shell electrons. For an ECR ion source, the first requirement is met by confining electrons and ions in a volume by magnetic fields. The magnetic field used on an ECR ion source is a combination of a radial field with an axial field. The magnetic field strength is a minimum in the center of the plasma chamber and increases in every direction from the center, a so called 'minimum B-field' configuration. For this

source, the radial field is obtained from hexapole permanent magnets which are made of SmCo magnetic material. The field strength is 5 kGauss at the inner wall of the plasma chamber. The axial magnetic field is supplied by two water-cooled solenoid coils. The mirror ratio is the ratio of the maximum field strength at the magnetic mirror to the field strength at the center of the source. The higher mirror ratio, the better plasma confinement is, and the better the chance to produce highly charged ions. Our source reaches a mirror ratio of 1.35 when the coil current is 400 Amps. The second condition to produce highly charged ions is met by injecting 5 GHz microwave into the plasma chamber to heat up electrons. Electrons are accelerated or decelerated by the electric field component of the microwave, and are doing cyclotron motion around the magnetic field lines inside the source. Once the electron cyclotron frequency is equal to the electric field oscillating frequency (microwave frequency), the electronic cyclotron motion becomes resonant (ECR). The intensity of the output ion beam increases with the injected microwave power.

A positive voltage (extraction voltage, HV) which can go up to 10 kV is applied on the plasma chamber; the rest of the beam line is at ground potential. An ion which loses its axial confinement sees the potential difference between the plasma chamber and the beam line. It will follow the field and be accelerated out of the source with energy of $(HV \times Q)$ keV.

Charge state selection Ions coming out of the source are first momentum analyzed by a 25 degree magnet (curvature radius R=16.5 inches). Later, they are deflected into the collision region by a 60 degree magnet (R=12 inches). This 60 degree

magnet not only deflects ions into the collision region but also cleans up ions which have undergone charge-exchange with background gas after the 25 degree magnet.

Beam-optic elements (Fig. 2.2) The design of this system is to have a slowly moving ion beam with reasonable beam intensity in the collision region. The collision count rate is proportional to the particle density, because the effective ion density is inversely proportional to its velocity, this system thus tries to enhance the ion density by slowing down the ion beam. The following section is going to describe the beam-optic elements in our collision system. In the section of the collision region, we will discuss how we decelerate an ion beam in the collision region. In appendix A , we have the computer simulations of beam transport in our ECR and EBIS beam lines.

- Source einzel lens: It is an electrostatic lens for focusing ion beams. It is a combination of three cylindrical tubes with their inner diameters (ID)= 2.125 inches, outer diameters (OD)=2.375 inches. The gap between the cylindrical tubes is 0.25 inches and the length of each tube is 2.1375 inches. A negative high voltage is applied to the center element. The front and back elements are grounded.
- Heynick deflector: It is an electrostatic octopole-deflector for steering ion beams in vertical and horizontal directions. Its ID is 3.0 inches; length is 6.25 inches.
- Electrostatic quadrapole triplet (EQ1,EQ2): They are electrostatic lenses for focusing ion beams. Each quadrapole consists of four cylindrical electrodes. A quadrapole will focus an ion beam in one direction and defocus it in another

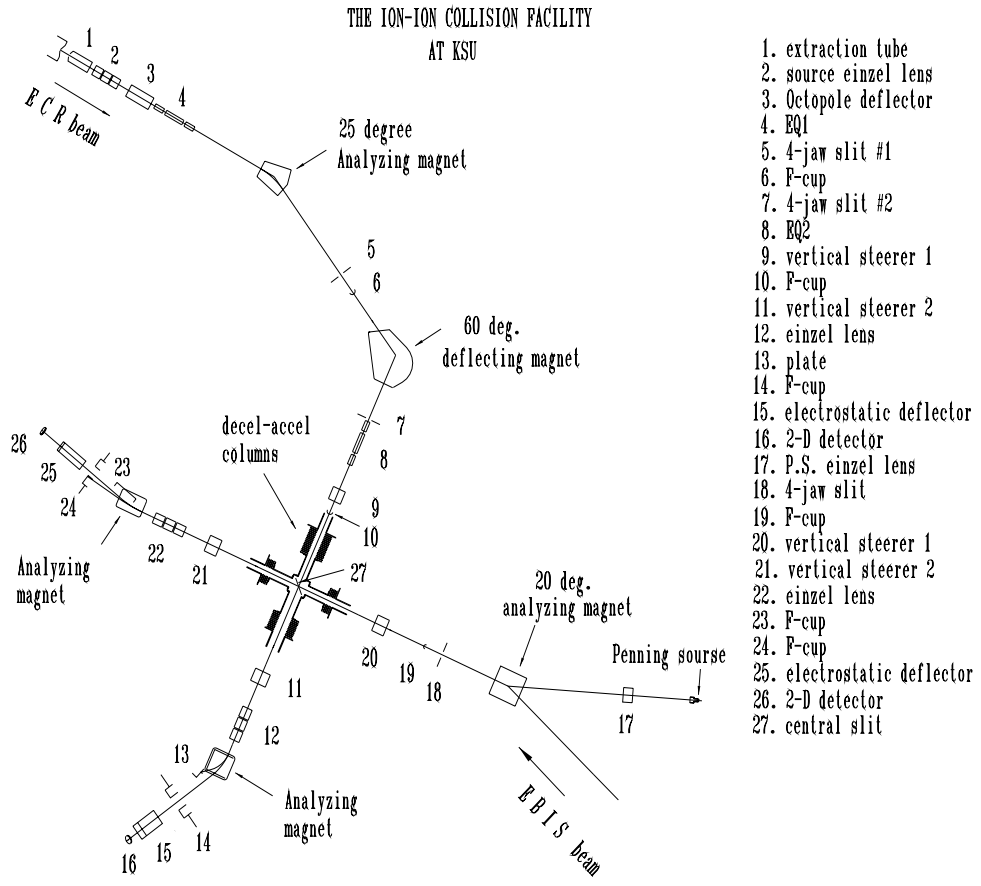


Figure 2.2: The beam-optic elements in the collision system

direction. With a combination of three quadrupoles (quadrupole triplet), an ion beam can be focused on horizontal and vertical planes separately. The distance between the pole tips is 1.18 inches, the electrodes are 2.4 inches long in the first and the third quadrupole, while those in the second quadrupole are 4.8 inches long.

- **Steerer1:** It is an electrostatic steerer for steering beams in the vertical direction.

Besides optical elements, there are also two sets of 4-jaw slits before the collision region to control the divergence and intensity of an ion beam at downstream of the beam line.

2.3.2 EBIS beam line

Source A small Penning ion source is used to produce singly charged ions. Ions are produced in a gas discharge in this source. The accelerating voltage which can go up to 10 kV is applied on the body (anode) of the source. The discharge voltage which can be varied between 0-3 kV is applied across the anode and the gas feed (cathode). The source is at positive high voltage, and the rest of the beam line is at ground potential. An ion coming out of the source has an energy of $[(\text{accelerating voltage} - \text{discharge voltage}) \times Q]$ keV in our setup.

Charge state selection Ions from the Penning ion source are momentum analyzed by a 20 degree magnet, then they are directed into the collision region.

Beam-optic elements Penning Source Einzel lens (P.S. lens): it is a single element einzel lens with ID= 3.34 inches, length= 2.34 inches. A positive voltage is applied to this lens.

2.4 Collision region

One major difficulty in all ion-ion collision experiments is the thin target density from an ion beam. For example: a 100 nA He^+ ion beam with energy 1 keV and cross section $1\text{ mm} \times 1\text{ mm}$ has a particle density of about 10^6 particles/cm³ similar to the residual gas density in an ultra high vacuum (10^{-10} torr) chamber at room temperature. The experimental difficulties associated with the thin ion density are low signal count rate and poor signal-to-background ratio. To overcome these difficulties, at first, we keep the collision region under ultra high vacuum (10^{-10} torr) conditions to reduce the residual gas density. The second approach is to use electrostatic, multi-element decel-accel columns in the collision region to retard ion beams in order to enhance the target ion density. The third experimental technique is to observe time-coincidences to differentiate true signals from background events. Another advantage coming of the decel-accel columns is the reduction of background events. Because the collision region is biased with high voltages, those background collision products generated before or after the collision region will have energies equal to the initial energies of the primary ions. Those collision products generated within the decel-accel columns will have energies different from the initial energies of the primary ions. Because of this energy label we can set up the electrostatic deflectors to allow

only those collision products from the collision region instead of from the whole beam line to reach to the detectors. In this way, background events on the detectors can be greatly reduced.

2.4.1 Decel-Accel columns

The decel-accel columns are four series of cylindrical symmetric rings mounted inside a 10 inch 6-way cross chamber in the collision region. Each ring is 0.125 inches thick, and has ID=2.063 inches except those on the ECR exit side which have ID=3.068 inches. The reason for making the inner diameter in the ECR exit large is to make sure that the angular acceptance in our system is sufficient for reaction products to get out of the collision region. Each ring is separated from the other by ceramic balls (OD=0.375 inches). The space between two rings is 0.2795 inches. In the ECR beam line, the column consists of 15 electrodes on the entrance, and 10 electrodes on the exit. In the EBIS beam line, it consists of 4 electrodes on both sides. The voltage increases linearly from the first entrance electrode to the center of the collision region, then decreases linearly to the exit. The full length of the collision region is about 38 cm long so as to keep the collision region field free in order that the overlap of ion beams can be measured without altering the ion optics.

2.4.2 Central slit

There are four different sizes of apertures made on two pieces of stainless steel plate inside the collision region as shown in Fig. 2.3. They are: a hole 2 mm in diameter,

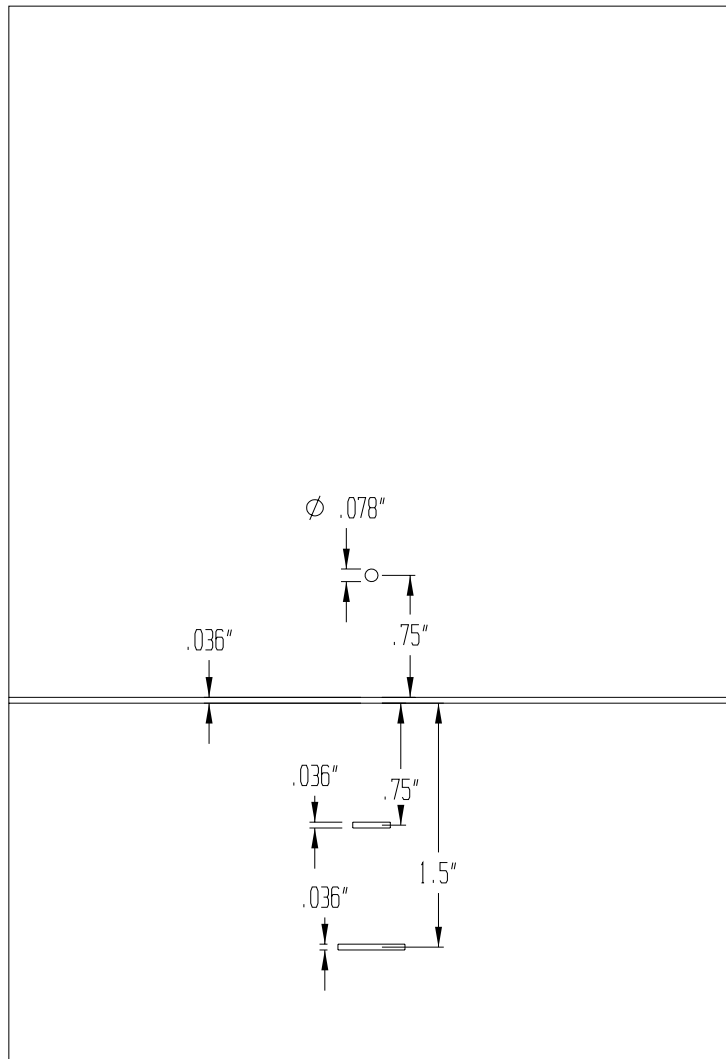


Figure 2.3: The design of the central slit

and 3 single slits having the same height (0.9144 mm) but different width (5.6896 mm, 10.16 mm, 110 mm). They are all aligned in vertical direction. The vertical distance between two apertures is 0.75 inches. They are movable only in one (vertical) direction. The motion of these apertures is controlled by a stepper motor controller which can be remote controlled by a computer program [59]. All these apertures are positioned 45 degrees with respect to each beam. The 2 mm diameter hole can be used to center ion beams horizontally . The single slits can be used to center ion beams vertically as well as to maximize ion beams through them. By scanning a single slit in the vertical direction, both of the beams' profiles can be probed simultaneously, and the form factor, which corresponds to the overlap of the ion beams can be determined.

2.5 After collision

A magnet and an electrostatic analyzer are used in each beam line to analyze charged particles. A magnet analyzes ions according to the momentum per charge of the ions, while an electrostatic analyzer analyzes ions by the energy per charge of the ions. In this setup, the analyzing magnets deflect ions in the horizontal direction, and the electrostatic analyzers deflect ions in the vertical direction. In each beam line, the primary ions are separated from the charge-changed ions by an analyzing magnet soon after they come out of the collision region. The primary ions are collected in a Faraday cup; the current measured in a cup is sent to a current integrator which digitizes the current by a unit charge per pulse. The collision products are further

analyzed by an electrostatic analyzer downstream and detected on microchannel-plate based position-sensitive detectors at the end of the beam lines.

2.5.1 ECR beam line

The size and position of the primary ion beam can be checked by a third set of 4-jaw slits in front of the analyzing magnet.

Analyzing system

- Analyzing magnet: It is a 30 degree analyzing magnet with $R=11.80$ inches.
- Electrostatic analyzer: It is a 45 degree cylindrical symmetric deflector. The central radius is 9 inches, and the gap between the two electrodes is 2 inches. It has very strong focusing in the radial (vertical) direction.

Beam-optic elements

- Steerer2: It is an electrostatic vertical steerer.
- Einzel lens: It is a three-element lens with $ID= 2.75$ inches, tube length= 2.5 inches and the gap between two of the tubes= 0.28 inches. A negative high voltage is applied to the central element; the first and the last elements are grounded. By using this einzel lens, the collision products can be well focused on the detector.

Detection system The ECR detector is a combination of two Galileo microchannel plates (41.91 mm diameter \times 1.02 mm thickness) which are placed in a stack, a wedge-strip type of anode, and a layer of grid which has about 90 percent transmission. A negative high voltage is applied to the front of the channel plate stack and a ground potential is connected to the back of the stack. The layer of grid which is about 1 inch above the front of the channel plate stack is at ground potential. A +50 volt potential is applied to the anode's Germanium layer in order to attract electron clouds from the channel plates. The anode gives three output voltages(X,Y,R) for each ion impact signal. These contain the position information about where the ion hits the detector.

2.5.2 EBIS beam Line

Analyzing system

- Analyzing magnet: It is a 15 degree analyzing magnet with R=24.12 inches.
- Electrostatic analyzer: It is a 20 degree cylindrical symmetric analyzer with 1.25 inch gap and 20 inch central radius. It has weak focusing in the radial (vertical) direction.

Beam-optic elements The same design as used in the ECR beam line.

- Steerer2: It is an electrostatic vertical steerer.
- Einzel lens: It is a three-element lens with tube ID= 2.75 inches, tube length=2.5 inches and the gap between two tubes = 0.28 inches. A negative high voltage

is applied to the central element; the first and the last elements are grounded.

This einzel lens is used to focus collision products on the detector.

Detection system The structure and operation are the same as described in the ECR detector section, except that the EBIS detector has 3 microchannel plates (40.2 mm diameter \times 1.02 mm thickness) in a stack.

Chapter 3

Electronics Scheme

The electronic arrangement for our ion-ion collision experiments are drafted in Fig. 3.1.

After collisions, the collision products are detected on a two-dimensional position-sensitive detector operating in single-particle counting mode at the end of each beam line. The detector has been described in the section of the detection system in Chapter 2.

For each particle hit, the backgammon anode of each detector will give three output signals which are (X,Y,R) from the three parts (wedge, strip, meander) of the anode. These signals contain the information of where the particle hits the detector. These signals are first preamplified by a CATSA (preamplifier), then further amplified and pulse-shaped by amplifiers. Finally, these signals are sent to an analog-to-digital converter (ADC) where they are processed and recorded on a computer through a CAMAC crate interface.

The timing signal is taken from the CATSA. It is first amplified by a fast timing amplifier, then is sent to a constant fraction discriminator. The noise on the detector can be properly cut off by the discriminator. The timing signal from one of the detectors is used to start the time-amplitude-converter (TAC), the timing signal from the other detector is used to stop the TAC. The output voltage from the TAC is proportional to the time difference between the start and the stop signals. Whenever the TAC generates an output signal, it will also generate a fast-value-conversion signal. This is sent to a gate generator. The ADC is then strobed by the output from the gate generator.

XSYS data acquisition and analysis package [60] is used to take and analyze our data.

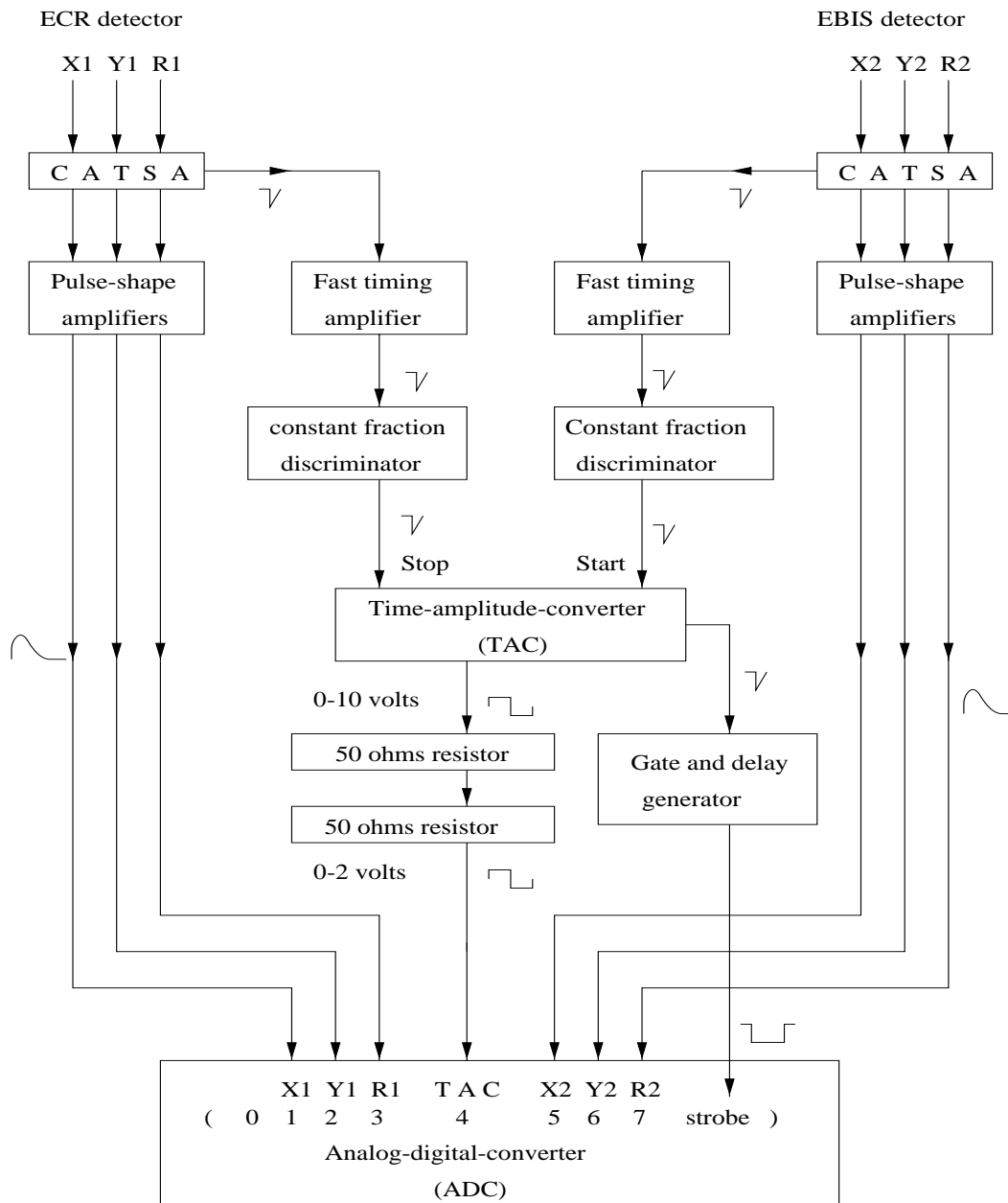


Figure 3.1: Electronics setup for the ion-ion collision experiments

Chapter 4

Data-Analysis

4.1 Data analysis

The total cross sections of charge exchange in ion-ion collisions are evaluated by the following equation:

$$\sigma = (R) \left(\frac{q_1 q_2 e^2}{I_1 I_2} \right) \left(\frac{v_1 v_2}{v_{rel}} \right) f$$

where

- R is the ion-ion collision count rate.
- e is the charge unit (1.6×10^{-19} coulomb).
- q_1, q_2 are the ion charges
- I_1, I_2 are the primary beam currents
- v_1, v_2 are the ion beam velocities in the laboratory frame.
- v_{rel} is the relative collision velocity of primary ion beams, and
- f is the form factor.

$$f = \frac{\int i_1(z) dz \int i_2(z) dz}{\int (i_1(z)i_2(z)) dz},$$

where $i_1(z)$ and $i_2(z)$ are the linear current densities of the ion beams at the vertical position z .

The following sections will discuss how these parameters are evaluated in our experiments.

Fig. 4.1 shows some typical spectra taken in our experiments. The figures labeled 'ECRXY' and 'EBISXY' are the images of the two-dimensional position-sensitive detectors at the end of the ECR and the EBIS beam lines respectively. The 'ALLTAC' spectrum shows all the time coincidences between the single signals 'ECRXY' and 'EBISXY'. The 'GTAC' figure is the time coincidence between those signals inside the software windows set on 'ECRXY' and on 'EBISXY'. The data shown in these figures is from the experiment He^{2+} on He^+ . The 10 keV He^{2+} beam was from the ECR ion source while the 5.55 keV He^+ beam was from the Penning ion source. The retarding voltage was set at +4 kV. Therefore, the particles detected on the ECR detector are He^+ with energy 6 keV, and those on the EBIS detector are He^{2+} with energy 9.55 keV. The particles detected on the detectors are both true signals and background.

Fig. 4.2 and Fig. 4.3 show the ion-ion collision signals on the ECR and EBIS detectors, respectively, after background subtraction. In Fig. 4.2, ECRX1 shows the ion-ion collision signals projected onto the detector X-position, and ECRY1 shows the projection onto the detector Y-position. Fig. 4.3 shows similar projections for the EBIS detector.

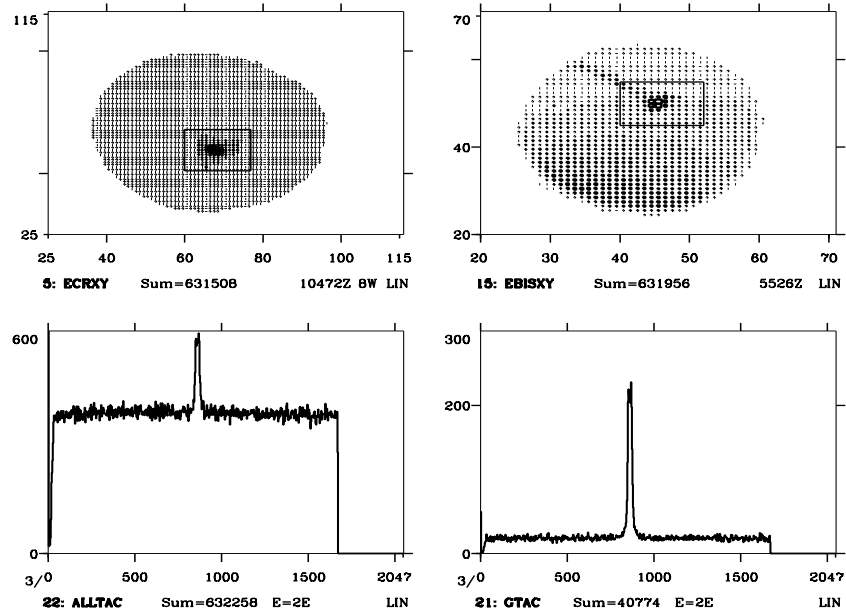


Figure 4.1: ECRXY: 2-D image of the ECR detector; EBISXY: 2-D image of the EBIS detector; ALLTAC: all of the time coincidences; GTAC: gated time coincidences.

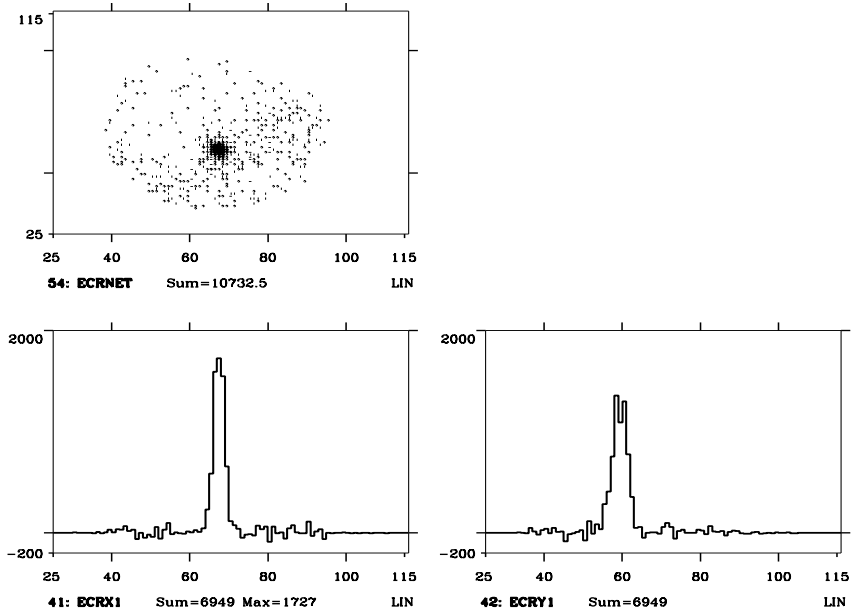


Figure 4.2: The true ion-ion collision signals on the ECR detector (background subtracted); ECRX1: signals on detector X-position; ECRY1: signals on detector Y-position.

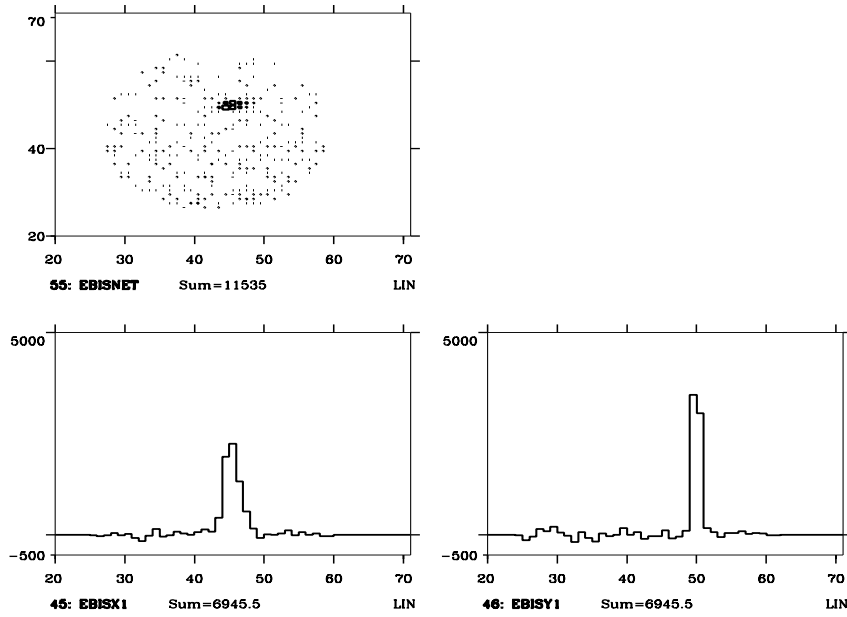


Figure 4.3: The true ion-ion collision signals on the EBIS detector (background subtracted); EBISX1: signals on detector X-position; EBISY1: signals on detector Y-position

As we have mentioned before, the count rate from ion-ion collisions (true signals) is much smaller than that from ion-residual gas collisions (background). Most of the particles detected on the detectors are therefore from background events. The time-coincidence technique is applied to differentiate the true signals from the background. Because the distance from the center of the collision region to each detector is fixed, only the particles coming from ion-ion collisions have a certain time-of-flight difference. Conversely, particles from background events come at random times. As we can see from the 'ALLTAC' spectrum in Fig. 4.1, a well defined peak emerges out of a flat random background. The area of the peak after background subtraction corresponds to the number of true events.

- Ion-Ion Collision Count Rate

$$N_{true} = N_{total} - N_{random}$$

where N_{total} , N_{true} , and N_{random} are the number of coincidences of total, ion-ion and background, respectively, within a TAC peak. Since the distribution of particle counting follows Poisson statistics, the number of random coincidences is therefore estimated by an exponential fit to the background distribution. The statistical uncertainty in N_{true} is

$$\sigma_N = \sqrt{N_{total} + N_{random}}$$

In reality, detectors have detection efficiency less than 100%. The N_{true} is the number of ion-ion coincidences measured with certain detection efficiency

from our detectors. The true number of ion-ion collision events (N_{real}) should therefore be corrected for our detection efficiencies, that is

$$N_{real} = \frac{N_{true}}{\epsilon_1 \epsilon_2}$$

where ϵ_1 and ϵ_2 are the detection efficiencies of our ECR and EBIS detectors, respectively. We have measured our ECR and EBIS detector detection efficiencies *in situ*. (see Appendix C.) Their measured values are $(38.29 \pm 2.75)\%$ for each detector.

The difference between the 'ALLTAC' and 'GTAC' spectra is that the random uncertainty in 'GTAC' is much smaller than that in the 'ALLTAC' spectrum, but the number of ion-ion coincidences under the TAC peak in each spectrum is the same. The cross sections and the relative errors in the data are evaluated from the 'GTAC' spectrum.

- Current

The primary ion beams are collected in Faraday cups. A digital current integrator is used to digitize the ion beam current. It gives a +5V output pulse for every C coulombs of input charge, where C is the range setting on the integrator. The number of pulses output from the current integrators are accumulated throughout the experiment and recorded on a computer. Thus, the average current, I , can be calculated as

$$I = \frac{(the\ total\ number\ of\ pulses) \times (C\ coulomb)}{(data\ taking\ time)}$$

- Form Factor f

Fig. 4.4 shows an example of the beam profiles in the collision region. The FWHM (full width at half maximum) of the ECR beam is typically about 1 mm and that of Penning beam is about 2 mm. The form factor f which characterizes the spatial overlap of ion beams along the vertical axis is given by

$$f = \frac{\int i_1(z) dz \int i_2(z) dz}{\int (i_1(z)i_2(z)) dz}$$

where $i_1(z)$ and $i_2(z)$ are the linear current densities of the ECR and Penning ion beams at position z , respectively.

Generally, the ion beam densities are probed by moving a central slit ($0.9144 \times 110 \text{ mm}^2$) in the vertical direction at 0.0254 mm per step through both beams. Since the slit intersects both beams at 45 degrees, both of the ion beams through the slit can be measured simultaneously downstream in Faraday cups at each vertical position. The form factor f can then be calculated by using the formula above. In an ideal case which both ion beams are uniform, the form factor is just the width (in the vertical direction) of the larger beam.

During an experiment, ion beams will drift and cause the form factor to change during the data taking time. The relative variation of the form factor can be as much as 10%. This is larger than the statistical uncertainty from the coincidence measurement and becomes a dominant uncertainty source. However, experiments can be carried out with the central slit ($0.9144 \times 5.6896 \text{ mm}^2$) set at the vertical centers of both the ion beams. With the central slit set at the

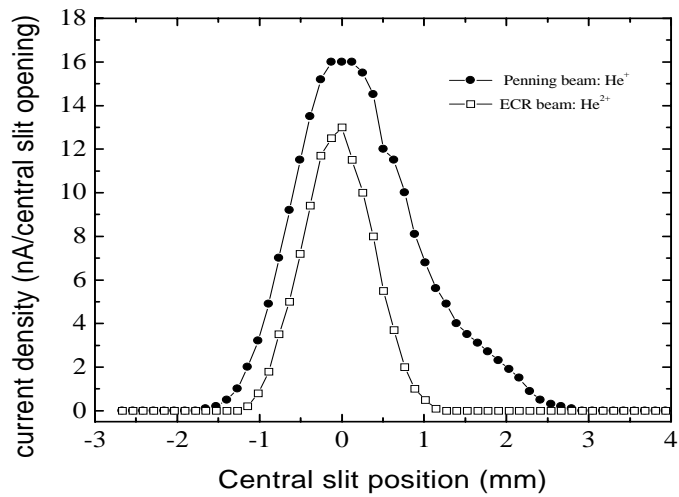


Figure 4.4: Form factor measurement: linear current density vs central slit position

vertical centers of the ion beams, the form factor is then determined only by those portions of the ion beams which pass through the central slit. The form factor is then approximately equal to the height of the central slit (0.9144 mm). Experiments had been carried out with the central slit in and out of beam positions to make sure that the total cross sections were not affected by the existence of the slit.

The most difficult parameter to determine in the evaluation of the total cross section is the number of true events. Because of the existence of angular scattering in ion-ion collisions, we have to be sure that we have collected all the ion-ion collision products. We had repeated the measurements with different settings on vertical steerer2 (to check the angular acceptance in the vertical direction), the post-collision analyzing magnet (to check the angular acceptance in the horizontal direction), and the post-collision einzel lens in each beam line to be sure that the total cross sections did not depend on beam optics.

The current measurement had also been verified by scanning the magnetic field and by varying the suppression voltage at the front of the cup to get a constant reading. This demonstrated that current was completely collected in a cup and that the secondary electrons were well suppressed.

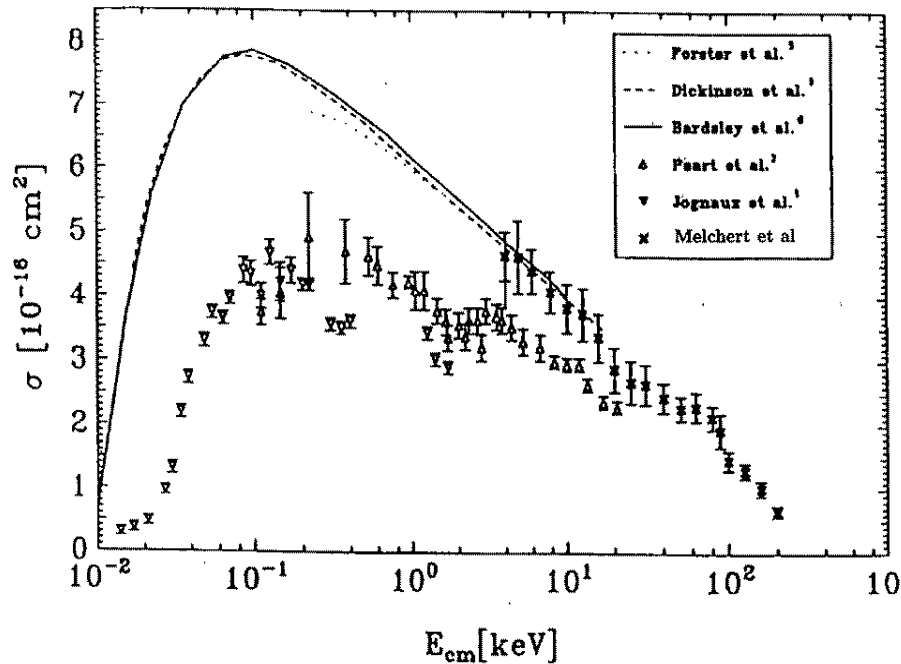


Figure 4.5: The energy dependence of the total cross sections of single charge exchange in $He^{2+} - He^+$ collisions [49].

4.2 Results and discussions

4.2.1 Single charge-exchange in $He^{2+} - He^+$ collisions

This one-electron, symmetric charge exchange system, He^{2+} on He^+ , has been heavily studied both experimentally [47–50] and theoretically [42–46] Fig. 4.5 [49] shows the results of the energy dependence of the total cross sections either measured or calculated by different groups. In theory Bates and Boyd [42] in 1962 published the first calculation for He^{2+} on He^+ by using the perturbed stationary-state approximation (PSS). Dickinson and Hardie [43] employed the two-state perturbed stationary-

state approximation but with accurate potentials of the *gerade* and *ungeraded* molecular states of He_2^{3+} . Forster *et al* [45] used the semi-classical impact-parameter method with a basis of atomic orbitals modified by plane-wave translation factors. Bardsley *et al* [46] applied the impact-parameter method combined with an approximate molecular-energy difference from the asymptotic interaction theory. The cross sections from different calculations are all in very good agreement with each other. In experiments, a tentative result was reported by Brouillard and Delfosse [61] in 1967. About ten years later, Jognaux *et al* [47] measured the total cross sections for center of mass energies ranging from 0.01 keV to 1.7 keV by using a merged beams method. About the same time, Peart and Dolder [48] also carried out their measurements from 0.1 keV to 20 keV by using an intersecting beams method. Both of the results were below the theoretical calculations. The discrepancy between theory and experiment was due to insufficient angular acceptance for collecting all the reaction products [49]. The colliding ions repel each other along their incoming and outgoing trajectories. Only recently were the measurements carried out by Melchert *et al* [50] at E_{cm} ranging from 4 keV to 200 keV in very good agreement with theory. We then tried to test our system by measuring the total cross sections for this collision system at center-of-mass energies (E_{cm}) ranging from 1.775 keV to 14.775 keV to compare with existing calculations and measurements. Our results as well as the data measured by Melchert *et al* [50] are plotted in Fig. 4.6 for comparison. They are also tabulated in Table 4.1. Some of our experimental parameters are listed in Table 4.2 for reference.

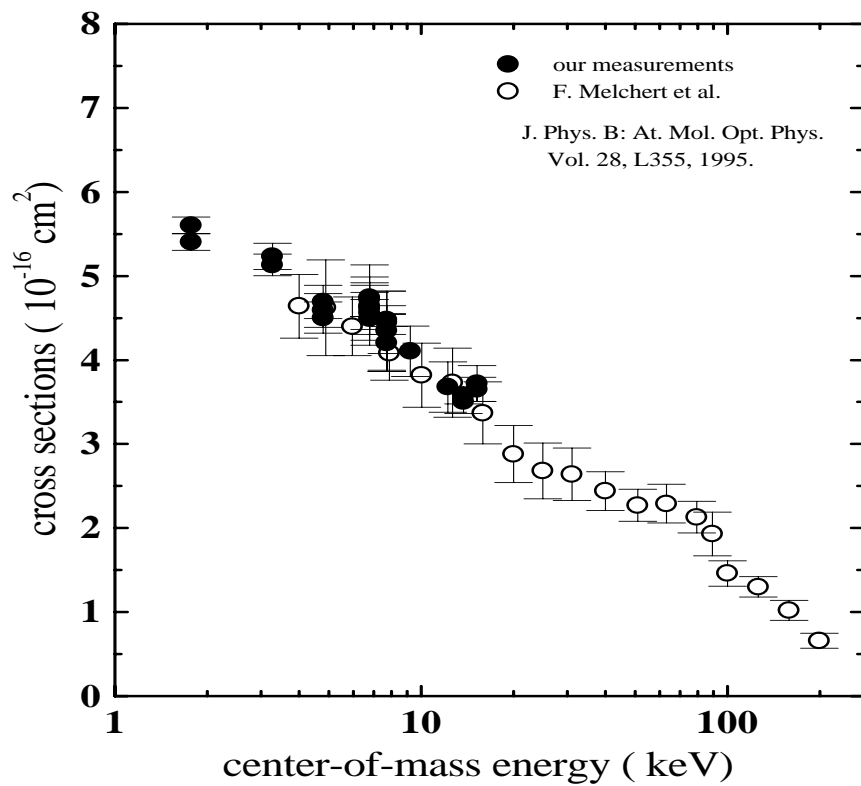


Figure 4.6: The energy dependence of the total cross sections of single charge-exchange in $He^{2+} - He^+$ collisions

E_{cm} (keV)	1.775	3.275	4.775	6.775	7.725	9.225	12.225	13.725	15.225
σ (10^{-16} cm^2)	5.60 ± 0.10	5.23 ± 0.16	4.59 ± 0.20	4.65 ± 0.34	4.45 ± 0.37	4.11 ± 0.30	3.68 ± 0.30	3.51 ± 0.14	3.65 ± 0.14

Table 4.1: Our cross section measurements for He^{2+} - He^+ collisions.

E_{cm} (keV)	$E_{He^{2+}}$ (keV)	E_{He^+} (keV)	$V_{retarding}$ (kV)	$I_{He^{2+}}$ (nA)	I_{He^+} (nA)	ECR single rate (1/sec.nA)	EBIS single rate (1/sec.nA)	time (sec)
1.775	10	5.55	+4	5.0	24.2	500	132	52,955
4.775	10	5.55	+2	6.0	17.2	450	140	19,012
15.225	14	7.45	-3	9.2	24.0	1,185	158	76,830

Table 4.2: Experimental parameters for He^{2+} - He^+ collisions

For the $He^{2+} - He^+$ collision system the cross sections calculated by theory is for resonant charge transfer between the ground state of $He^+(1s)$ and He^{2+} . Historically, the contamination of metastable states in the projectile ion beam has always concerned experimental atomic physicists. The existence of metastable states can substantially affect the capture cross sections in ion-atom collisions [62]. Therefore, before making any comparison of our data to others, we need to examine the condition of our He^+ beam. After investigating our system, we conclude that the metastable state of $He^+(2s)$ has already been quenched after the He^+ ions come out of the Penning ion source (see discussions in Appendix B.). The cross sections we measured were indeed the resonant charge transfer in collisions between the ground state of $He^+(1s)$ ions and He^{2+} bare ions. Then, from the Fig. 4.6, we can see that the data

from our experiment is in very good agreement with those measured by Melchert *et al.*, which demonstrates that our ion-ion collision system is working!

4.2.2 Single charge-exchange in $Ne^{2+} - Ne^+$ and $Ar^{2+} - Ar^+$ collisions

Besides the $(He^{2+} - He^+)$ collision system, we have also measured the total cross sections for single charge-exchange for the $(Ne^{2+} - Ne^+)$ and $(Ar^{2+} - Ar^+)$ systems at $E_{cm} = (1.775 - 10.775)$ keV and $(2.775 - 7.275)$ keV, respectively. Some typical experimental parameters for $Ne^{2+} - Ne^+$ collisions are listed in Table 4.3. The cross sections measured at different collision energies for these two collision systems are listed in Table 4.4 for $Ne^{2+} - Ne^+$ collisions and Table 4.6 for $Ar^{2+} - Ar^+$ collisions. The one-electron potential model calculations are also listed in other tables, Table 4.5 for $Ne^{2+} - Ne^+$ collisions and Table 4.7 for $Ar^{2+} - Ar^+$ collisions. The energy dependence of the total cross sections is plotted in Fig. 4.7 for $Ne^{2+} - Ne^+$ collisions, in Fig. 4.8 for $Ar^{2+} - Ar^+$ collisions. Fig. 4.9 shows the energy dependence of all the total cross sections of these three collision systems on the same plot.

The experimental measurements of the total cross sections for $(Ne^{2+} - Ne^+)$ and $(Ar^{2+} - Ar^+)$ are about a factor of 1.3 and 2.7, respectively, larger than those measured in the $(He^{2+} - He^+)$ system.

E. Sidky and I. Reiser [63] have applied a one-electron potential model code to calculate the total cross section for resonant single charge transfer in $(Ne^{2+} - Ne^+)$

E_{cm} (keV)	$E_{Ne^{2+}}$ (keV)	E_{Ne^+} (keV)	$V_{retarding}$ (kV)	$I_{Ne^{2+}}$ (nA)	I_{Ne^+} (nA)	ECR count rate (1/sec.nA)	EBIS count rate (1/sec.nA)	time (sec)
1.775	10	5.55	+4	11.5	38.0	835	174	51,259
4.775	10	5.55	+2	10.0	39.0	580	128	52,548
10.775	10	5.55	-2	10.0	34.0	540	88	38,892

Table 4.3: Experimental parameters for $Ne^{2+}-Ne^+$ collisions

E_{cm} (keV)	1.775	3.275	4.775	6.775	9.275	10.775
σ ($10^{-16} cm^2$)	6.83 ± 0.14	6.66 ± 0.34	6.60 ± 0.19	5.60 ± 0.19	5.32 ± 0.21	5.35 ± 0.19

Table 4.4: Experimental measurements for $Ne^{2+}-Ne^+$ collisions

E_{cm} (keV)	2.5	4.025	4.775	5.5	6.25	8.0	10.0	20.0
σ ($10^{-16} cm^2$)	7.61	7.4	6.48	6.77	6.42	6.20	5.89	5.04

Table 4.5: One-electron potential model calculations for $Ne^{2+}-Ne^+$ collisions

E_{cm} (keV)	2.775	3.525	4.275	5.025	6.525	7.275
σ ($10^{-16} cm^2$)	16.89 ± 0.19	16.96 ± 0.52	15.10 ± 0.67	13.34 ± 0.19	13.41 ± 0.49	13.46 ± 0.65

Table 4.6: Experimental measurements for $Ar^{2+}-Ar^+$ collisions

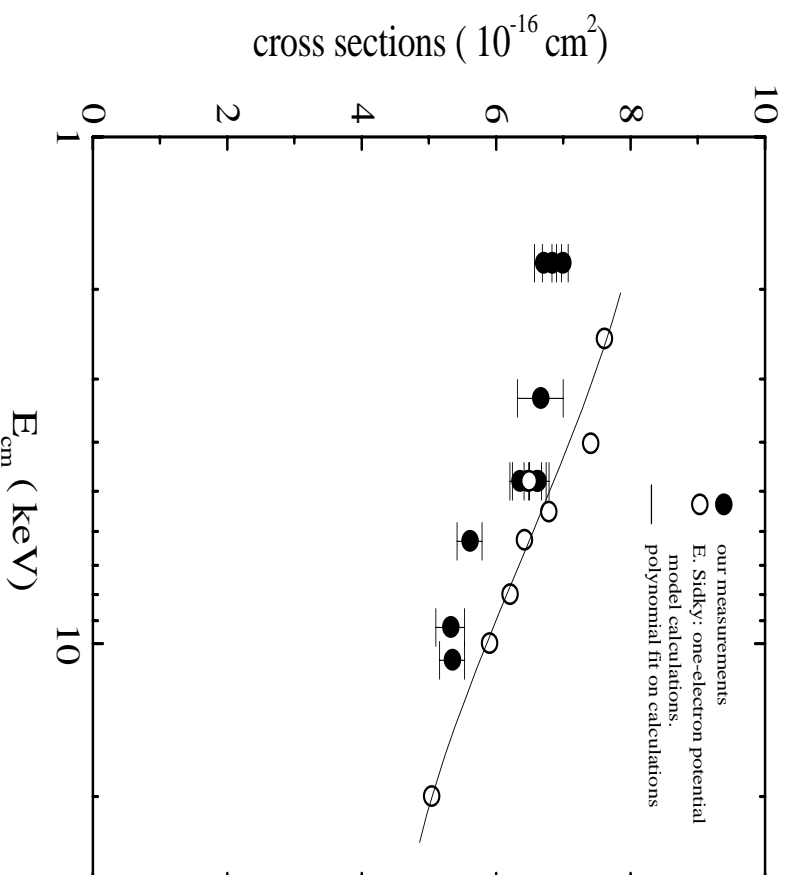


Figure 4.7: The energy dependence of the total cross sections of single charge-exchange in $Ne^{2+} - Ne^+$ collisions

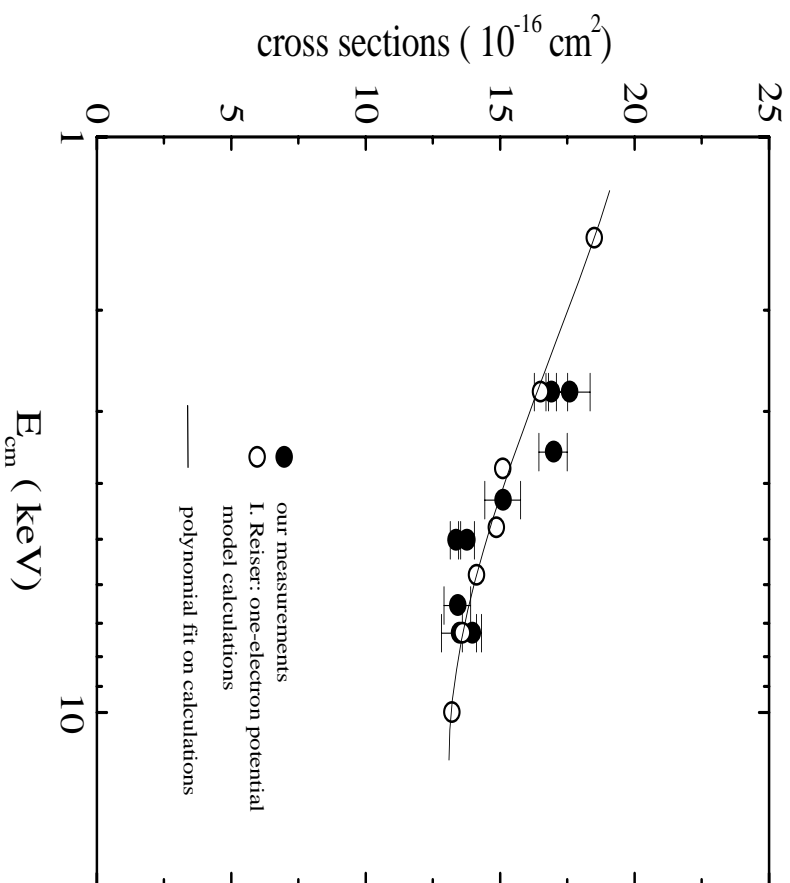


Figure 4.8: The energy dependence of the total cross sections of single charge-exchange in $Ar^{2+} - Ar^+$ collisions

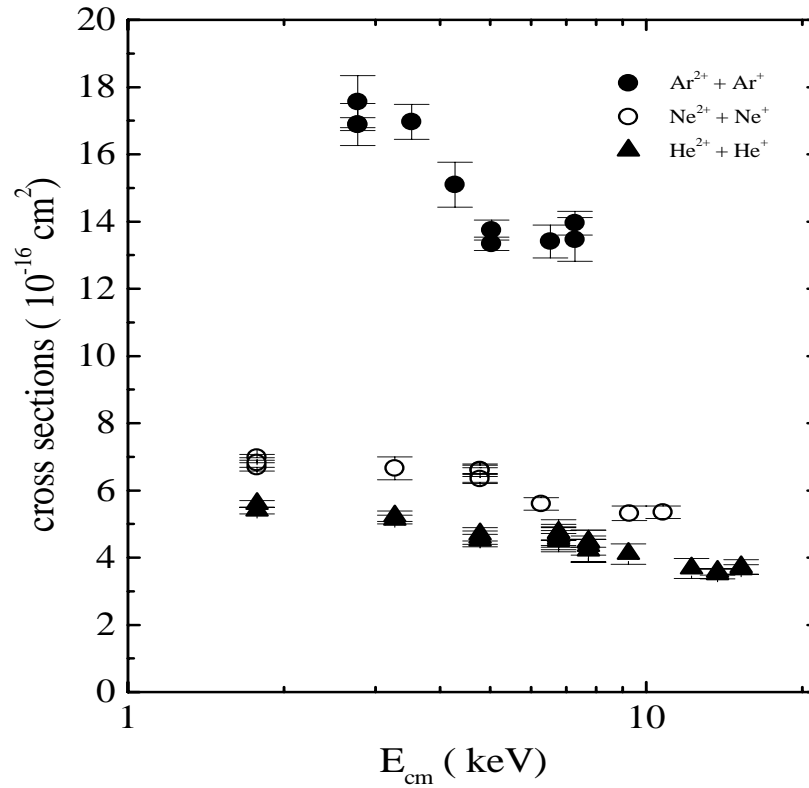


Figure 4.9: The energy dependence of the total cross sections of single charge-exchange in $Ar^{2+} - Ar^+$, $Ne^{2+} - Ne^+$ and $He^{2+} - He^+$ collisions.

E_{cm} (keV)	1.5	2.775	3.775	4.775	5.775	7.275	10.0
σ (10^{-16} cm^2)	18.477	16.481	15.077	14.84	14.097	13.579	13.183

Table 4.7: One-electron potential model calculations for Ar^{2+} - Ar^+ collisions and ($Ar^{2+} - Ar^+$) collisions. In the calculations, the projectile nuclei are assumed to follow classical straight line trajectories, and a basis set of atomic orbital states is used to describe the electron wave functions. The electron to be captured by the projectile ion is considered to be only one of the five electrons in the p orbital of the target ion. The ionic cores of the projectile and target ions are assumed to be structureless. Because the active electron is in the p state, there are three substates, which are $m_l = 1, 0, -1$, for each p state. In the calculations these substates are assumed to be equally populated and the total cross section is the average of all the cross sections from these three substates. The results from the simple one-electron potential model calculations are shown on the same figures with our experimental data for comparison.

As mentioned in the previous discussion for the $He^{2+} - He^+$ collisions, metastable states can sometimes play an important role in determining the cross sections of electron capture in ion-atom collisions. We know that our ECR ion source can possibly create $Ne^{2+}(Ar^{2+})$ ions in their metastable states. The possible low-lying metastable states of $Ne^{2+}(Ar^{2+})$ and their ionization energies are listed in a table in Fig. 4.10. We know that the electric field strength in our system is not strong enough to quench

these metastable states if they are populated. Furthermore, these metastable states have long lifetimes. For example: the life time of $Ar^{2+}(^1S)$ is about 109 ± 32 ms [64]. This means that our Ne^{2+} (Ar^{2+}) ions in the collision region may include ions in metastable states. If this is true, then there are many possible channels open in these single capture collision processes. The possible initial and final channels are plotted in Fig. 4.10. We have ignored the fine structure of the 2P Ne^+ ion, which is quite small, and show only the different energy levels for the Ne^{2+} ion. From the plot we see that there are three resonant channels like $Ne^+ + Ne^{2+}(^3P_2) \rightarrow Ne^{2+}(^3P_2) + Ne^+$ and some other non-resonant channels like $Ne^+ + Ne^{2+}(^1D_2) \rightarrow Ne^{2+}(^3P_2) + Ne^+$. Even though there might have many channels open in collisions, the dominant channels for symmetric charge transfer at low collision energies are the resonant channels. The resonant charge exchange process in ion-atom collisions had been investigated very much both theoretically and experimentally in the 1960's and 1970's [65]. A two-state, straight-line impact-parameter approximation has been developed to describe the capture probability and the total cross section of resonant charge exchange in ion-atom collisions. The capture probability at impact velocity v and impact parameter b can be expressed as

$$P(v, b) = \sin^2 \left[\int_{b_{min}}^{\infty} \{E_g(R) - E_u(R)\} \frac{R}{v\sqrt{R^2 - b^2}} dR \right]$$

where b_{min} is the closest approach of the nuclei, E_g and E_u are the eigen-energies of the *gerade* and *ungerade* ionic molecular eigen-functions at internuclear distance R . The total cross section is

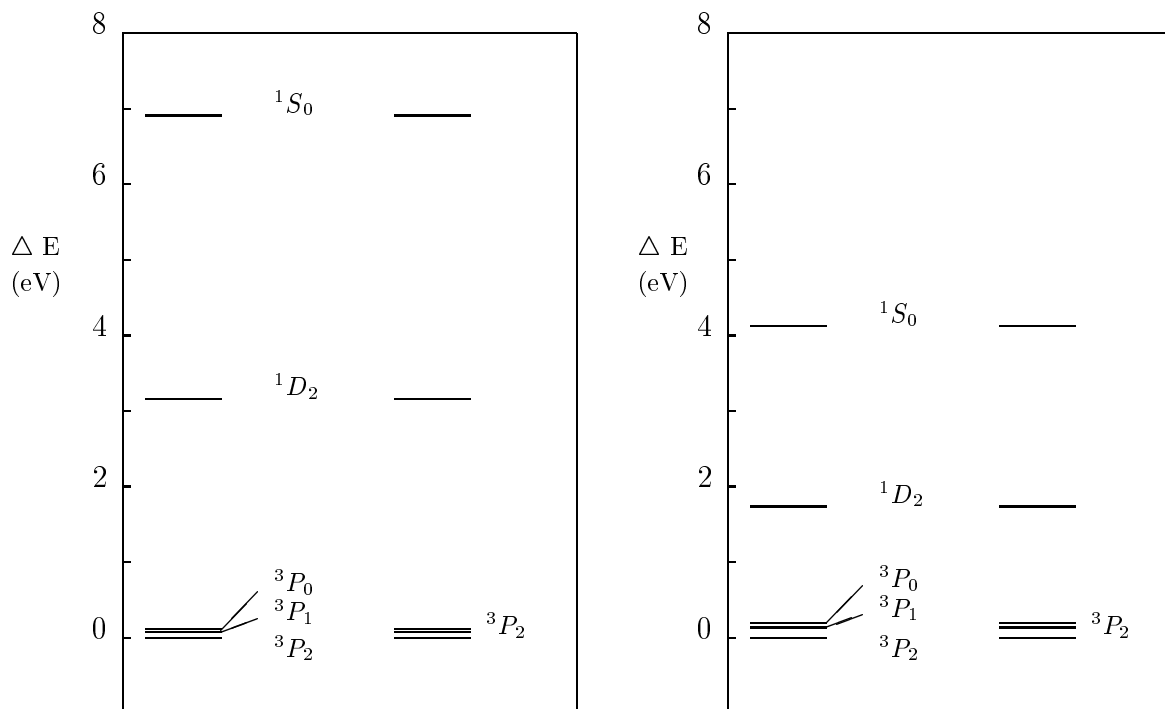
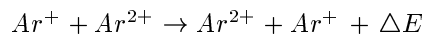
$$\sigma = 2\pi \int_0^{\infty} bP(v, b)db$$

The capture probability oscillates rapidly between zero and one for values of b less than a value of b_0 , then decreases exponentially for $b > b_0$. In a first approximation the $P(v,b)$ can be replaced by an average value of 0.5 for $b \leq b_0$, and taken to be zero for $b > b_0$, then $\sigma = \frac{1}{2} \pi b_0^2$, where b_0 is the largest impact parameter at which $P(v,b)$ assumes a certain small value [65]. The cross section then becomes geometrical, determined by the b_0 value. A more extended analysis by J. B. Hasted and M. A., D. Phil. [66] showed that the total cross section could be expressed as

$$\sigma^{1/2} = A - B \ln v$$

where v is the impact velocity, A and B are constants both of which depend on the ionization potential of the target atom; and the total cross section gets larger when the ionization potential value gets smaller for a fixed impact velocity. Based on this approximation, the capture cross section for any one of the three resonant channels in $Ne^{2+} - Ne^+$ collisions is the same as the other two because the ionization potential of the target ion, Ne^+ , is the same in all three channels. As a result, the percentage of metastable states populated in the main beam, Ne^{2+} , does not matter in determining the total cross section for the single resonant charge-exchange process in $Ne^+ - Ne^{2+}$ collisions. The same argument can be applied to $Ar^+ - Ar^{2+}$ collisions. For the reasons presented in the preceding two paragraphs, resonant charge exchange cross sections are basically, geometrically determined and not dependent on other structure or coupling parameters. This explains why a good agreement is found between our measurements and the one-electron potential model calculations which do not distinguish the capture cross section for any one of the channels from any

other. From this approximation we can also understand why the total cross section for $He^{2+} - He^+$ is not much different from that for $Ne^{2+} - Ne^+$, but is very different from that for $Ar^{2+} - Ar^+$. The reason is that the ionization potential of He^+ (54.4 eV) is not much different from Ne^+ (41.07 eV) but is very different from Ar^+ (27.62 eV). Alternatively, the effective b_0 , which corresponds roughly to the internuclear distance at which *gerade* and *ungerade* orbitals begin to split, is about the same for He^+ on He^{2+} and Ne^+ on Ne^{2+} , but much larger for Ar^+ on Ar^{2+} .



Ne^+	$I_p(V)$	Ne^{2+}	$I_p(V)$	Ar^+	$I_p(V)$	Ar^{2+}	$I_p(V)$
$(2s^22p^5)$		$(2s^22p^4)$		$(3s^23p^5)$		$(3s^23p^4)$	
$^2P_{3/2}$	41.07	3P_2	63.75	$^2P_{3/2}$	27.62	3P_2	40.90
$^2P_{1/2}$	40.97	3P_1	63.67	$^2P_{1/2}$	27.44	3P_1	40.76
		3P_0	63.64			3P_0	40.71
		1D_2	60.55			1D_2	39.16
		1S_0	56.84			1S_0	36.78

I_p : ionisation potential

Ground state of Ne^{2+} : $2s^22p^4(^3P_2)$

Ground state of Ar^{2+} : $3s^23p^4(^3P_2)$

Figure 4.10: The energy level diagrams for single charge-exchange in $Ne^{2+} - Ne^+$ and $Ar^{2+} - Ar^+$ collisions

Chapter 5

Concluding Remarks

In this dissertation, we have implemented a 90 degree crossed-beam ion-ion collision facility in the J. R. Macdonald laboratory. The system has been tested by measuring the total cross sections for single charge-exchange in $He^{2+} - He^+$ collisions at center of mass energies ranging from 1.775 keV to 14.775 keV. Our measurements are in very good agreement with existing experimental data as well as theoretical calculations. In addition to the $He^{2+} - He^+$ experiment, we have also performed experiments to measure the energy dependence of the total cross sections for single charge-exchange in $Ne^{2+} - Ne^+$ and $Ar^{2+} - Ar^+$ collision systems. The total cross sections of $Ar^{2+} - Ar^+$ and $Ne^{2+} - Ne^+$ collisions are about a factor of 2.7 and 1.3, respectively, larger than those of $He^{2+} - He^+$ collisions. These results are also in very good accord with one-electron potential model calculations. This agreement suggests that the single charge-exchange process in symmetric ion-ion collision systems at low collision energies is dominated by resonant charge-transfer processes. Also, trajectory effects do not play

an important role in determining the total cross sections of single charge-exchange for these collision energies.

With this new system, the following future research is possible: First, one could measure angular differential cross sections of ion-ion collisions in order to provide more stringent tests on theoretical models. Second, one could study ion-ion collisions between two multiply charged ions an area which is still not well explored to date.

Appendix A

Beam Optics Calculations

In this chapter we used a pc program, SIMION [67], to simulate the beam optics in our ECR and EBIS beam lines.

In the ECR beam line, we simulated a primary ion beam, 10 keV He^{2+} , starting from the second set of 4-jaw slits after the 60 degree magnet to the center of the collision region which has a 4 kV potential. In the post-collision region, we simulated the charge changed beam, 2 keV He^+ , from the center of the collision region to the ECR detector.

In the EBIS beam line, the primary beam is 5.55 keV He^+ while the charge changed beam is He^{2+} with energy 1.55 keV inside the collision region.

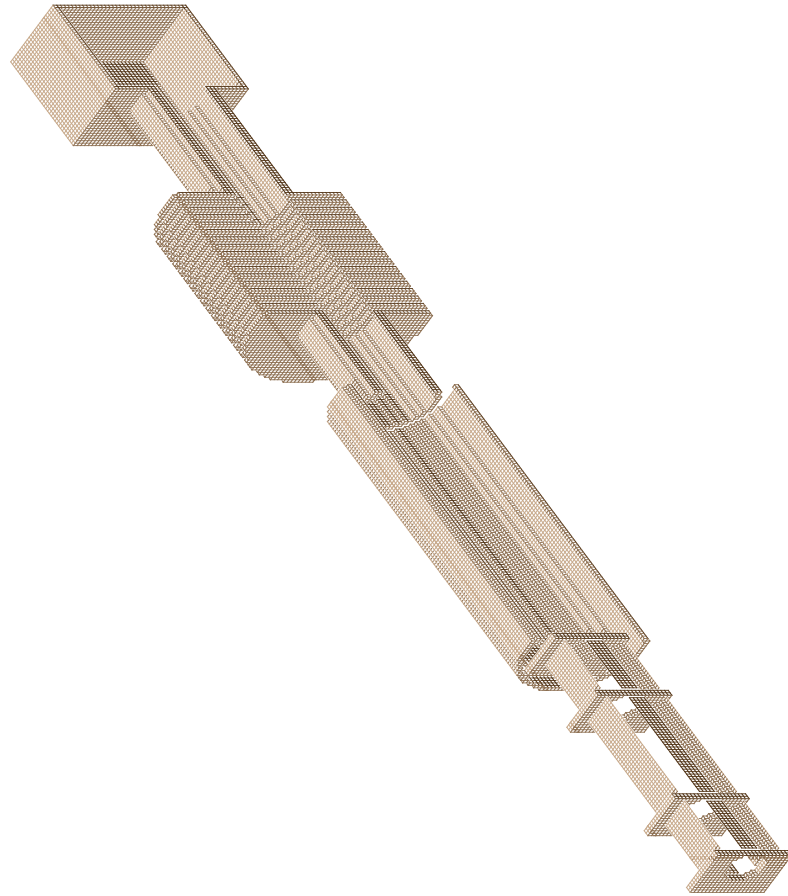
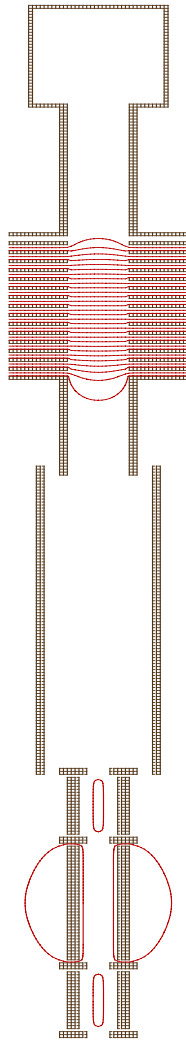


Figure A.1: 3-D plot of the ECR beam line: including the EQ1, the deceleration column and the collision region.



NOIIMS

Figure A.2: A voltage contour plot of the ECR pre-collision region: $V_{retarding}=4$ kV;
 $V = \pm 95$ volts on quadrupole 1 and 3 ; $V = \pm 104$ volts on quadrupole 2.

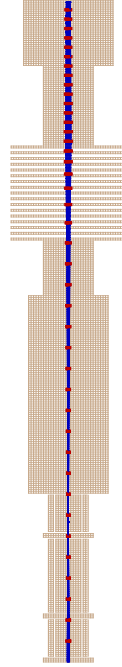
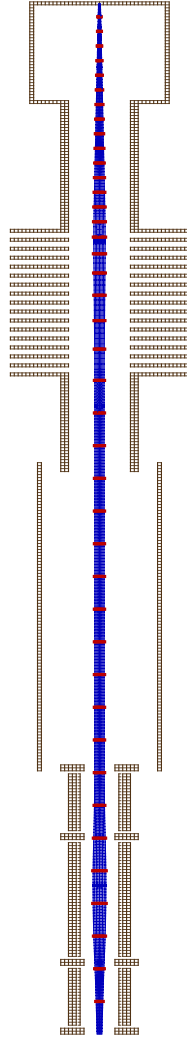
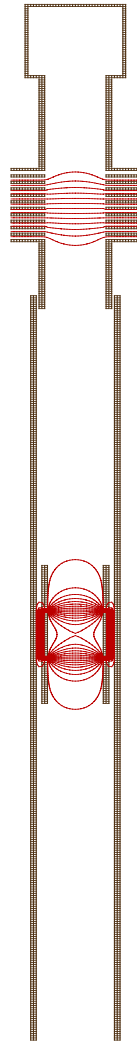


Figure A.3: Horizontal(X): ECR primary beam He^{2+} starts from the 2nd set of 4-jaw slits (bottom): He^{2+} : 10 keV, full width=3 mm, half angle= 0.2° , time marker: 50 nsec. The beam size at the center of the collision region is about 5.3 mm.



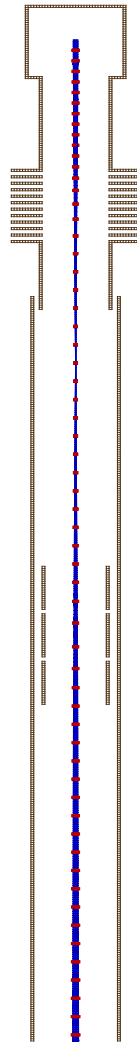
SIMION

Figure A.4: Vertical(Y): ECR primary beam He^{2+} starts from the 2nd set of 4-jaw slits (bottom): He^{2+} : 10 keV, full width = 4 mm, half angle= 1° , time marker: 50 nsec. The beam size at the center of the collision region is about 3.0 mm.



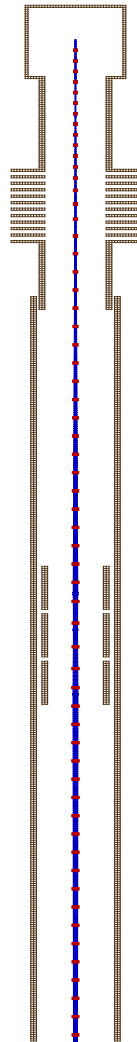
STIMION

Figure A.5: A voltage contour plot of the ECR post-collision region: $V_{retarding}=4$ kV, einzel lens:(-4.9 kV).



SIMION

Figure A.6: Horizontal(X):ECR charge-exchange beam He^+ starts from the center of the collision region (top): He^+ :2 keV, full width=5.3 mm, half angle= (-0.2408^0) , time marker:50 nsec. The beam size at the bottom of the plot (F-cup position) is about 6.7 mm.



SIMION

Figure A.7: Vertical(Y):ECR charge-exchange beam He^+ starts from the center of the collision region (top): He^+ :2 keV, full width=3 mm, half angle= (-0.84^0) , time marker:50 nsec. The beam size at the bottom of the plot(F-cup position) is about 11.4 mm.

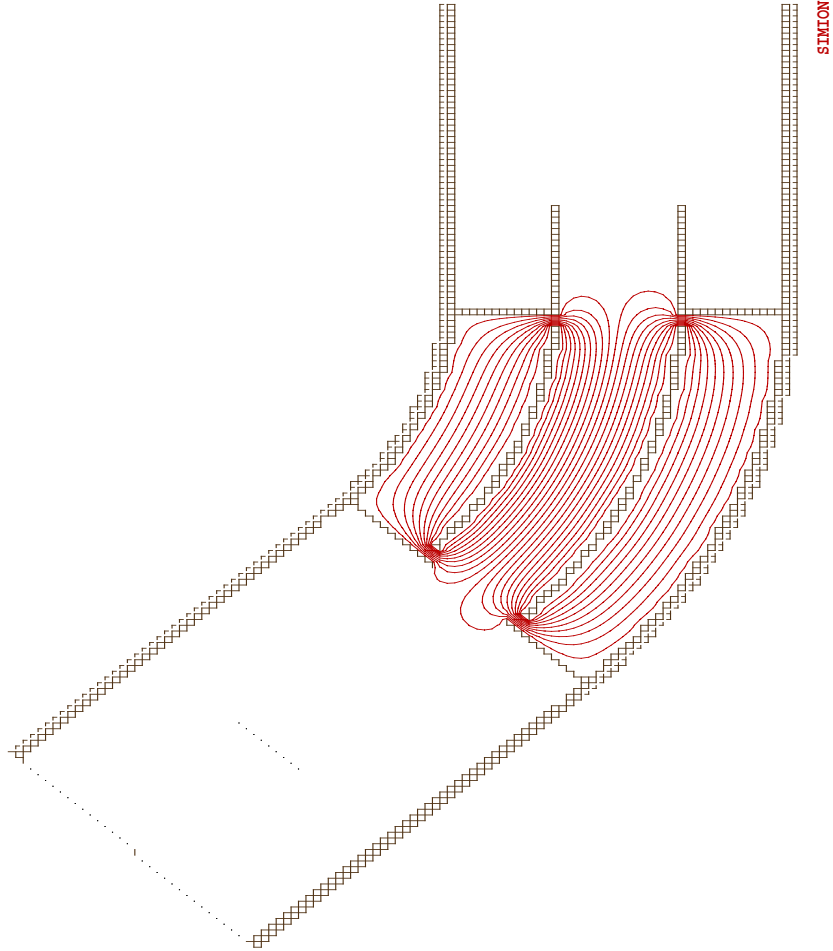


Figure A.8: A voltage contour plot of the ECR 45⁰ electrostatic deflector: $V = (\pm 1.5kV)$ on the plates.

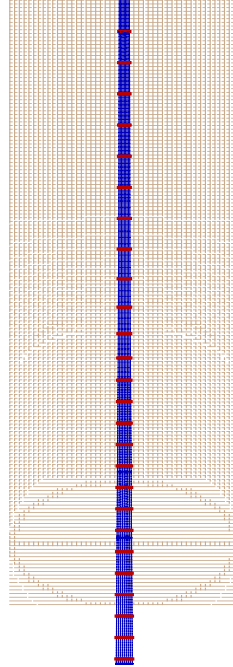


Figure A.9: Horizontal(X) : ECR charge-exchange beam He^+ starts from the F-cup
(top) : He^+ : 6 keV, full width= 6.7 mm, half angle = (0.1104^0) , time marker : 50
nsec. The beam size at the detector position is about 8.8 mm.

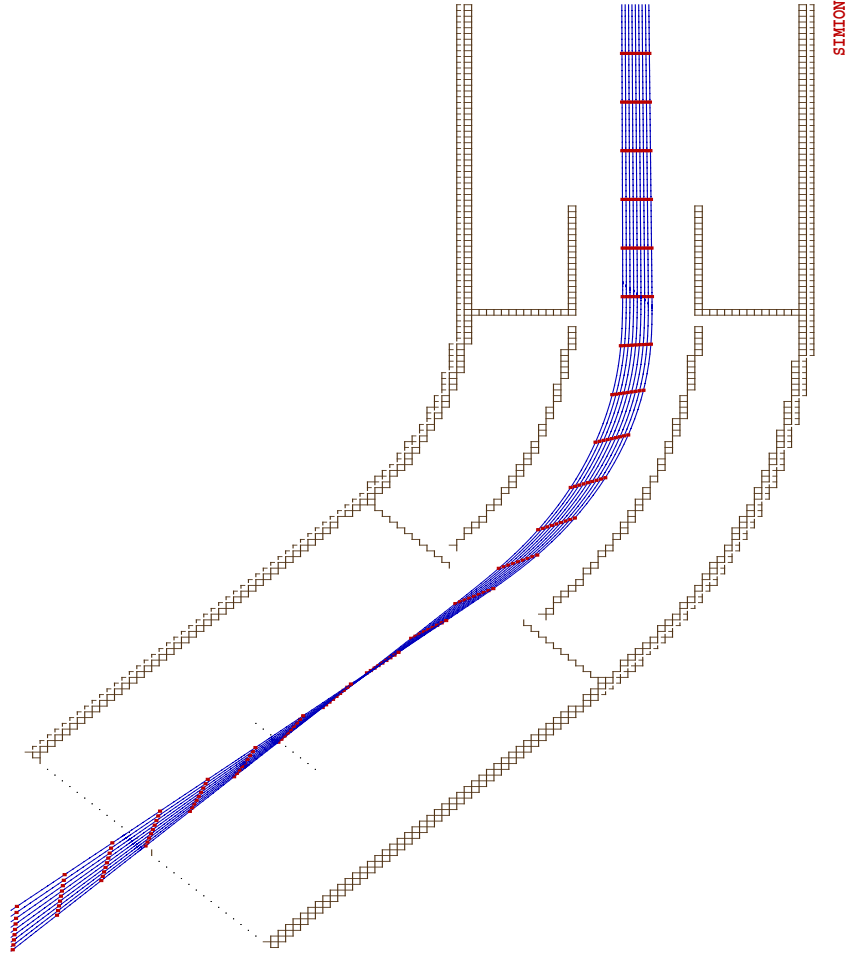
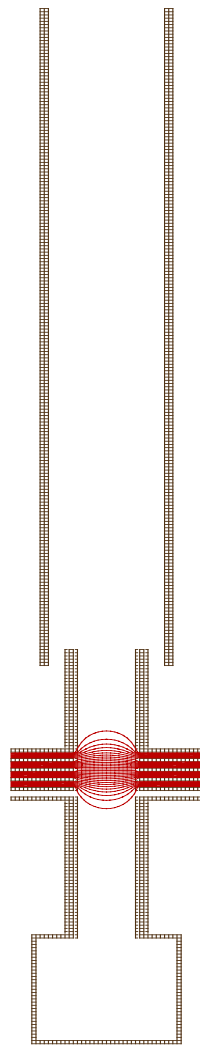


Figure A.10: Vertical(Y) : ECR charge-exchange beam He^+ starts from the F-cup
 (top) : He^+ : 6 keV, full width = 11.4 mm, half angle = (-0.15°) , time marker : 50
 nsec.



SIMION

Figure A.11: A voltage contour plot of the EBIS prior-collision region : $V_{retarding} = 4$ kV.

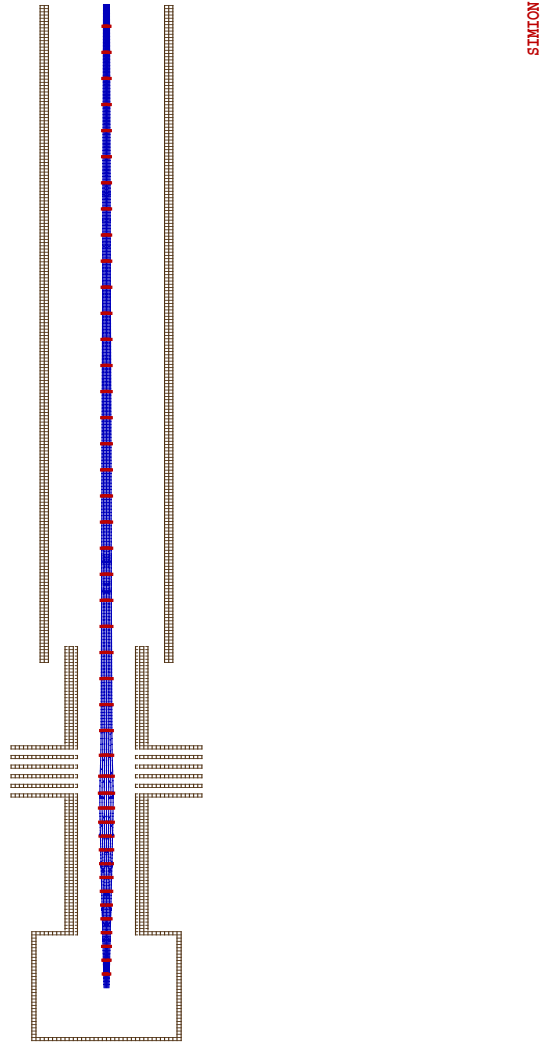
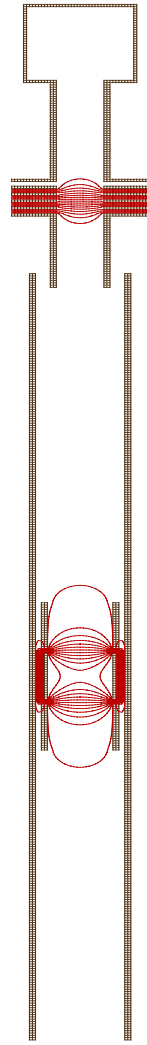
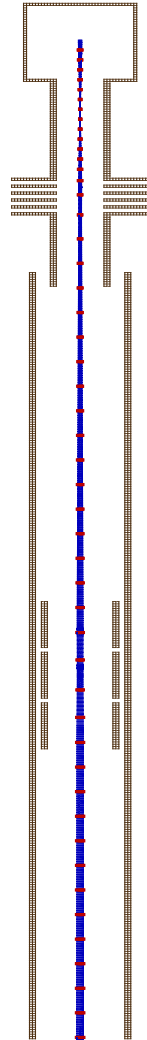


Figure A.12: EBIS Primary beam He^+ :trajectories are traced back from the center of the collision region(bottom) to the 4-jaw slit: He^+ :1.55 keV, full width=4 mm, half angle= (1.05^0) , time marker: 50 nsec. The beam size at the end of the plot(4-jaw slit) is about 4.5 mm.



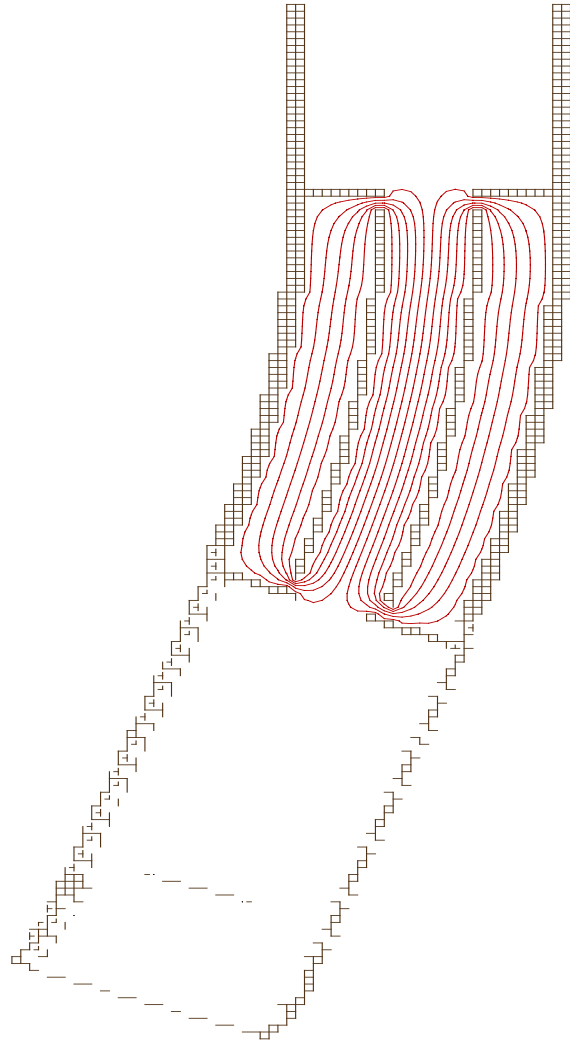
STIMION

Figure A.13: A voltage contour plot of the EBIS post-collision region: $V_{retarding}=4$ kV; einzel lens: (-2.9) kV.



SIMION

Figure A.14: EBIS charge-exchange beam He^{2+} starts from the center of the collision region (top) to the downstream F-cup: He^{2+} : 1.55 keV, full width=4 mm, half angle= (-1.05°) , time marker: 50 nsec. The beam size at the F-cup (bottom) is about 6.9 mm.



NOIWIIS

Figure A.15: A voltage contour plot of the EBIS 20⁰ electrostatic deflector: $V = (\pm 0.32 kV)$ on the plates.

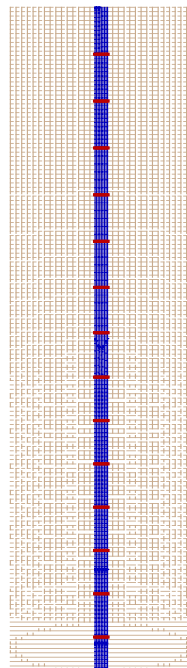


Figure A.16: Horizontal(X):EBIS charge-exchange beam He^{2+} starts from the F-cup
(top): He^{2+} :9.55 keV, full width=7.0 mm, half angle= (0^0) , time marker:50 nsec. The
beam size at the detector position is about 7.0 mm.

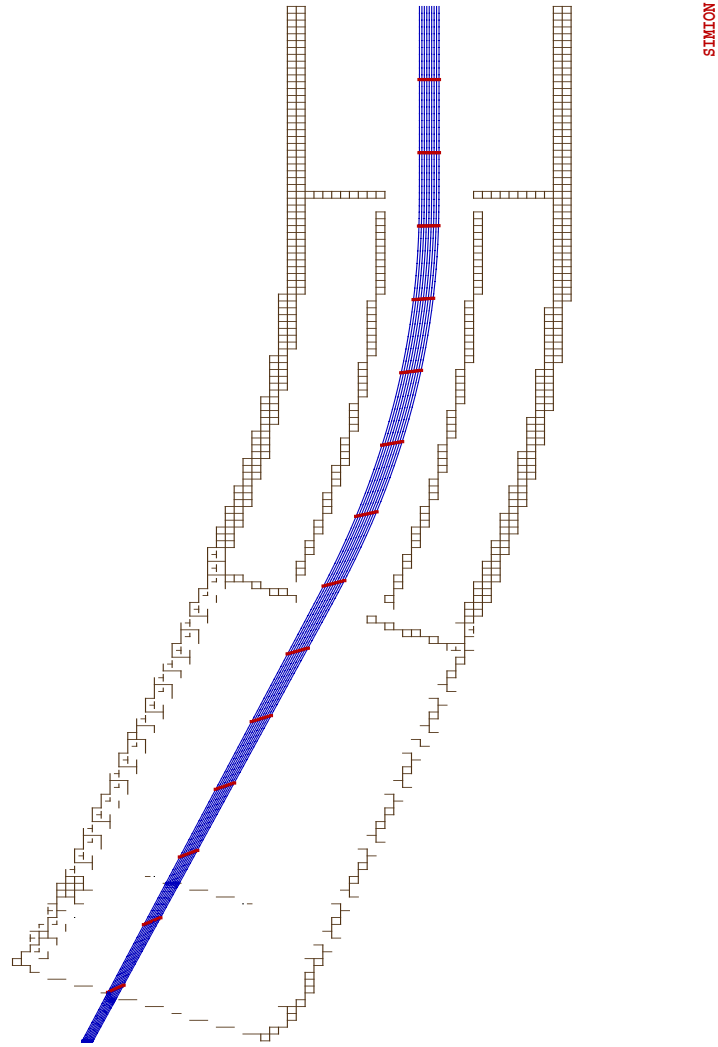


Figure A.17: Vertical(Y):EBIS charge-exchange beam He^{2+} starts from the F-cup
 (top): He^{2+} :9.55 keV, width=7.0 mm, half angle= (0^0) , time marker:50 nsec.

Appendix B

Lifetime Of He^+ Metastable States

Under the influence of an external electric field E (Stark effect), the eigenstate $|\psi\rangle$ of $He^+(n=2)$ forms an oscillating combination of $|2s\rangle$ and $|2p\rangle$ states. Thus, $|\psi\rangle$ can decay to the ground state $1s$ via its $2p$ component. In first-order perturbation theory, the lifetime of $|\psi\rangle$ is given as follow [68]:

$$\tau(\psi) = \frac{\tau(2p)Z^2(\Delta E(Lamb\ shift))^2}{3e^2E^2a_0^2}.$$

The lifetime $\tau(2p)$ of $He^+(2p)$ can be estimated from the following equation

$$\tau(Z) = \frac{1}{Z^4}\tau(Z=1),$$

where $\tau(Z=1)$ is the lifetime of the $2p$ state of atomic hydrogen H . Because the $\tau(Z=1)$ of the $H(2p)$ is about 1.6 nsec, the $\tau(Z=2)$ of the $He^+(2p)$ is then about 0.1 nsec. Furthermore, the Lamb shift $\Delta E(Lamb\ shift)$ of He^+ is 5.83×10^{-5} eV. The lifetime $\tau(\psi)$ of the $He^+(2s)$ beam is then only a function of the electric field strength(E), which yields

$$\tau(\psi) = \frac{162}{E^2} \text{ (sec)}, \text{ where } E \text{ is in unit of volt/meter.}$$

Before collisions, the He^+ beam will encounter electric fields at four different places. These are: between the source and the extraction tube, at the Penning source einzel lens, at the 20 degree analyzing magnet and at the deceleration columns. The electric field strength between the source and the extraction tube is $7.45kV/1.83cm$ for the high energy beam and $5.55kV/1.83cm$ for the low energy beam in our experiments. The lifetime $\tau(\psi)$ for these electric field strengths is about 0.98 nsec and 1.76 nsec , respectively. But, the flight time is about 30.6 nsec and 35.5 nsec , respectively. The flight time is much longer than the lifetime in either case. The metastable state of He^+ is thus already quenched when ions come out of the source. We therefore believe that the cross sections we measured for $He^{2+} - He^+$ are only those of the ground state resonant charge transfer process.

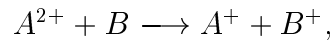
Appendix C

Detector Efficiency Measurements

The present work was motivated by the needs to determine the absolute detection efficiency of our ECR detector for singly charged ions(He^+ , Ne^+) with energies of 6 to $17keV$, and the detection efficiency of our EBIS detector for doubly charged ions(He^{2+} , Ne^{2+}) with energies of 3.55 to $9.55keV$. The principal technique applied in this work was same as the one published by Savin *et al* [69].

C.1 General theory

The count rate for electron capture process like



is given by

$$R_{A^+} = \epsilon \sigma \ln(p) \frac{I_{A^{2+}}}{2e},$$

where

- ϵ is the detector efficiency
- σ is the cross section of capture in a collision system,
- l is the interaction length between the projectile and gas target,
- $n(p)$ is the target density,
- $I_{A^{2+}}$ is the projectile current.
- e is charge unit(1.6×10^{-19} coulomb)

The relation between the target density $n(p)$ and gas pressure p can be found from the ideal gas law. It is

$$n(p) = \frac{p}{kT}$$

where k is the Boltzmann constant, and T is the temperature in Kelvin.

The change in the capture count rate can thus be expressed as a function of the change in gas pressure. It is

$$\Delta R_{A^+} = \epsilon \sigma l \left(\frac{\Delta p}{kT} \right) \left(\frac{I_{A^{2+}}}{2e} \right) \quad (\text{C.1})$$

When the capture count rate is very high, the capture products(A^+) can be collected in a Faraday cup in current mode. Now, equation (1) can be expressed in terms of current, it is

$$\Delta I'_{A^+} = \sigma l \left(\frac{\Delta p'}{kT} \right) \left(\frac{I'_{A^{2+}}}{2} \right) \quad (\text{C.2})$$

The detection efficiency of a Faraday cup in current measurements is 100%. When we combine equations (1) and (2), the detector efficiency in particle counting mode can be written as

$$\epsilon = e \left(\frac{I'_{A^{2+}}}{I_{A^{2+}}} \right) \left(\frac{\Delta R_{A^+}}{\Delta p} / \frac{\Delta I_{A^+}}{\Delta p'} \right). \quad (\text{C.3})$$

As we see in equation (C.3), the detector efficiency can be determined without knowing the absolute value of the capture cross section, the absolute pressure in the collision region or the exact target length. The only assumption in this approach is that the ion gauge response is linear over the pressure range of interest.

Due to some limitations of our system, we could not measure the EBIS detector efficiency for the doubly charged ions (He^{2+} , Ne^{2+}) with this technique. The reasons for not measuring our EBIS detector efficiency for He^{2+} is that the ionization cross section of ($He^+ - He$) at collision energies less than $10keV$ is very small. The charge current corresponding to the ionized projectiles is very small, and can not be measured accurately with our instruments. The reason for not being able to measure our EBIS detector efficiency for Ne^{2+} is that our Penning ion source can not produce enough Ne^{3+} projectile ions for experiments. The detector efficiency was therefore measured only for the singly charged ions instead of for the doubly charged ions. We can assume that the detector has same detection efficiency for doubly charged ions and singly charged ions over the same ion impact energies as long as the detection efficiency is constant over the energy range of interest. [70].

C.2 Setup

The detection efficiencies of our detectors were measured *in situ*- same apparatus and same detector settings as if we were running an ion-ion collision experiment.

A doubly charged ion beam extracted from an ion source was momentum analyzed before it went into the collision region. The gas target in the collision region was prepared by leaking gas into the vacuum chamber through a venting valve on the central turbo pump. The pressure inside the chamber was measured using a nude ion gauge (UHV I-NUDE-F by Duniway company). The ion gauge is expected to have a linear response from 10^{-10} to 10^{-4} torr. Since we wanted to monitor the pressure inside the vacuum chamber during the experiment, the retarding voltage in the collision region had to be turned off. Because of this, the interaction lengths on both beam lines became about 200cm in our experiments. After collisions, the primary projectile ions were separated from the capture projectile ions by a magnet. The primary projectile ions were collected in a Faraday cup. As to the capture projectile ions, they were detected on a detector in particle counting mode at very low target gas pressure (10^{-9} torr range). As the target gas pressure increased up to (10^{-6} torr range), the capture projectile ions were collected in a Faraday cup in current mode(capture current). We measured the projectile current at two different positions in each beam line for each pressure setting. One measurement was taken upstream from the collision region, the other downstream from the post-collision analyzing magnet. Current measured in a cup was carefully checked with the cup suppression voltage. At high pressure range, we noticed that current measured downstream of the

collision region was slightly smaller than the value measured upstream. This was due to an increase in capture and scattering events which occurred in the collision region. The capture count rate and capture current were thus normalized to the projectile current measured upstream of the collision region for each pressure setting.

C.3 Results and discussions

A typical plot of the normalized count rate vs the gas pressure is shown in Fig. C.1. Another typical plot of the normalized capture current vs the gas pressure is shown in Fig. C.2. A linear fit to the data is given on each figure. The measured detection efficiencies of our ECR and EBIS detectors are plotted in Fig. C.3 as a function of the beam energy. The uncertainties of the instruments and the statistical fluctuations involved in our current, pressure and count rate measurements had been taken into account (see table C.1). A quadrature sum of all these relative errors in each measurement yields the total relative error of the efficiency value (σ_i) [71]. The relative error (σ_i) of each efficiency value as shown in Fig. C.3 is less than 7%.

From the figure we can see that the detection efficiencies are quite constant over the beam energy range covered. The mean value ($\bar{\epsilon}$) of all the measurements (ϵ_i) are calculated as follows:

$$\bar{\epsilon} = \frac{\sum(\frac{\epsilon_i}{\sigma_i^2})}{\sum(\frac{1}{\sigma_i^2})}$$

the uncertainty in the $\bar{\epsilon}$ is

$$\sigma_{\bar{\epsilon}} = \sqrt{\frac{1}{\sum(\frac{1}{\sigma_i^2})}} = 0.43$$

count rate measurement σ_R :	$\frac{\text{standard deviation of } R}{\frac{\sqrt{(N=10)}}{\text{average of } R}} \approx 2.2\%$
projectile current measurement: σ_{I_p}	$\frac{\text{one half of the smallest scale division}}{\text{total reading}} \approx 2.6\%$
current of the charge changed particles: σ_{I_c}	$\frac{\text{one half of the smallest scale division}}{\text{total reading}} \approx 3.8\%$
pressure measurement: σ_p	$\frac{\text{one half of the smallest scale division}}{\text{total reading}} \approx 1.1\%$
<p>The detector efficiency is calculated as follows:</p> $\epsilon = e \left(\frac{I'_{A^{2+}}}{I_{A^{2+}}} \right) \left(\frac{\Delta R_{A^+}}{\Delta p} / \frac{\Delta I_{A^+}}{\Delta p'} \right)$ <p>the total relative uncertainty in determining each ϵ is given as:</p> $\sigma = \sqrt{\sigma_{I_p}^2 + \sigma_{I_c}^2 + \sigma_R^2 + \sigma_{I_c}^2 + \sigma_p^2 + \sigma_p^2} \approx 5.93\%$	

Table C.1: The relative uncertainty of each variable measurement

and the standard deviation of the efficiency distribution is

$$\sigma = \sqrt{\frac{\sum(\epsilon_i - \bar{\epsilon})^2}{N-1}} = 2.75$$

From the calculations, we can determine our detector efficiency to be (38.29 ± 2.75) measurement, it is the effective efficiency of our detector which is a compound of microchannel plates and a layer of grid. In our detector, the open area ratio of the front microchannel plate is 50% according to the data sheet from the manufacturer Galileo company, and the transmission of the layer of grid is 90%. The detection efficiency of our detector would be 45% if evaluated from the geometric factors of the front microchannel plate and the layer of grid. The reason why our measured efficiency is smaller than 45% might be explained by the way our detector was operated. During experiments, a negative high voltage was applied to the front microchannel plate, but the layer of grid which was about 2cm above the front microchannel plate was at ground potential. Some

signals were not amplified because the secondary electrons generated near the open exit of a channel followed the electric field and escaped away from the microchannels. The effective efficiency of our detector is therefore smaller than 45%.

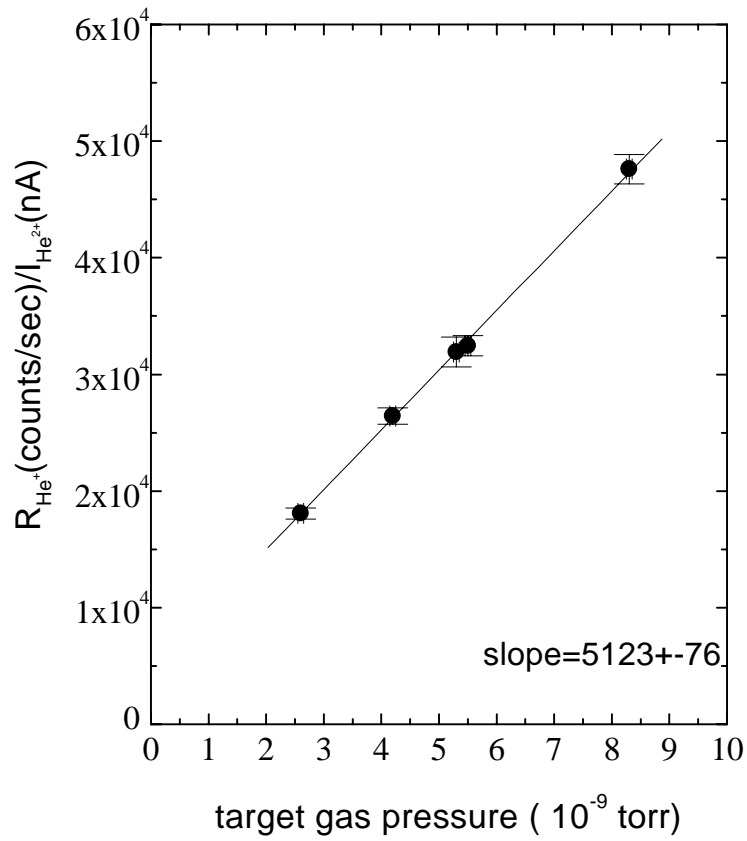


Figure C.1: The gas pressure dependence of the capture count rate

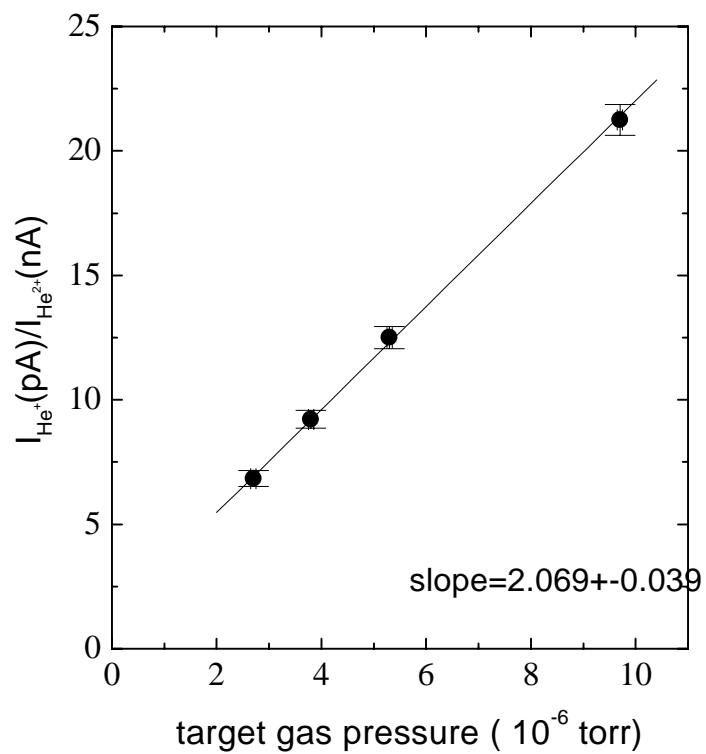


Figure C.2: The gas pressure dependence of the capture current

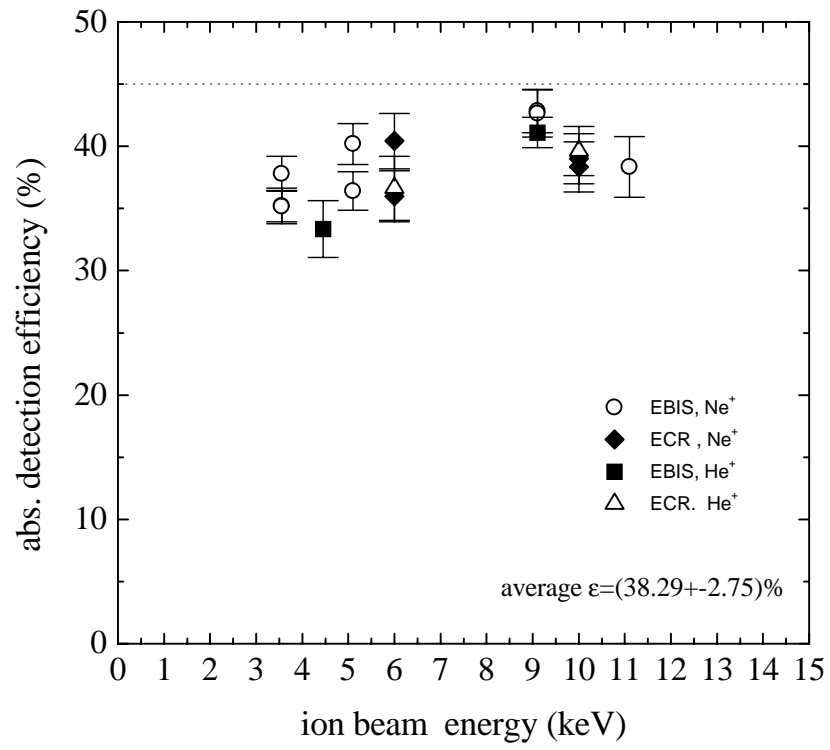


Figure C.3: The energy dependence of the detector detection efficiency

Bibliography

- [1] E. Salzborn, *Electron capture and ionization in ion-ion collisions*, J. Physique Coll., Volume C1, p.207 (1989).
- [2] K. F. Dunn, in *Atomic Processes in Electron-Ion and Ion-Ion Collisions*, edited by F. Brouillard., Plenum/New York, p.333-356 (1986).
- [3] K. Dolder and B. Peart, *Experimental aspects of two-body ion-ion collisions*, Rep. Prog. Phys., v.48, p.1283-1332 (1985).
- [4] H. B. Gilbody, in *Physics of Electronic and Atomic Collisions*, edited by S. Datz, published by North-Holland Publishing Company, p.223-234 (1982).
- [5] J. Tharamel and V. A. Kharchenko and A. Dalgarno, *Resonant charge transfer in collisions between positive ions*, Phys. Rev. A, V.50, p.496 (1994).
- [6] K. Dolder and B. Peart, in *Advances in atomic and molecular physics*, V.22, p.197-241 (1986).
- [7] K. Rinn and F. Melchert and E. Salzborn, *Measurements of charge transfer in $H^+ - He^+$ collisions*, J. Phys. B: At. Mol. Phys., V.18, p.3783 (1985).

- [8] K. Rinn and F. Melchert and K. Rink and E. Salzborn, *Ionisation in H^+ - He^+ collisions using an improved beam-pulsing technique for measuring the formation of He^{2+}* , J. Phys. B: At. Mol. Phys., V.19, p.3717 (1986).
- [9] J. B. A. Mitchell and K. F. Dunn and G. C. Angel and R. Browning and H. B. Gilbody, *Ionization and charge transfer in fast H^+ - He^+ collisions using an intersecting beam technique*, J. Phys. B: At. Mol. Phys., V.10, p.1897 (1977).
- [10] B. Peart and R. Grey and K. T. Dolder, *Measurements of cross sections for the formation of He^{2+} ions by collisions between protons and He^+* , J. Phys. B: At. Mol. Phys., V.10, No.13, p.2675 (1977).
- [11] G. C. Angel and K. F. Dunn and E. C. Sewell and H. B. Gilbody, *Ionisation and charge transfer in fast $H^+ - He^+$ collisions: further measurements of improved accuracy*, J. Phys. B: At. Mol. Phys., V.11, p.L49 (1978).
- [12] G. C. Angel and E. C. Sewell and K. F. Dunn and H. B. Gilbody, *Charge transfer and ionisation in fast $H^+ - He^+$ collisions: further measurements using a coincidence technique*, J. Phys. B: At. Mol. Phys., V.11, p.L297 (1978).
- [13] B. Peart and K. Rinn and K. T. Dolder, *Measurements of charge transfer and ${}^4He^{2+}$ production in collisions between protons and ${}^4He^+$ ions*, J. Phys. B: At. Mol. Phys., V.16, p.1461 (1983).
- [14] E. C. Sewell and G. C. Angel and K. F. Dunn and H. B. Gilbody, *Ionisation and charge transfer in fast H^+ - Li^+ collisions*, J. Phys. B: At. Mol. Phys., V.13, p.2269 (1980).

- [15] C. J. Hopkins and M. F. Watts and K. F. Dunn and H. B. Gilbody, *Measurement of cross sections for charge transfer in $H^+ - C^+$ collisions*, J. Phys. B: At. Mol. Phys., V.20, p.3867 (1987).
- [16] M. F. Watts and C. J. Hopkins and G. C. Angel and K. F. Dunn and H. B. Gilbody, *Charge transfer and ionisation in collisions of protons with Al^+, Ga^+, In^+ and Tl^+ ions*, J. Phys. B: At. Mol. Phys., V.19, p.3739 (1986).
- [17] J. G. Murphy and K. F. Dunn and H. B. Gilbody, *He^{2+} formation in collisions between fast He^+ ions*, J. Phys. B, V.27, p.3687 (1994).
- [18] B. Peart and R. A. Forrest and K. T. Dolder, *Measurements of cross sections for the formation of ${}^7Li^{2+}$ by collisions between ${}^7Li^+$ ions*, J. Phys. B, V.14, p.3457 (1981).
- [19] M. F. Watts and G. C. Angel and K. F. Dunn and H. B. Gilbody, *Charge transfer and ionisation in collisions between Li^+ ions*, J. Phys. B, V.17, p.1631 (1984).
- [20] B. Peart and R. A. Forrest and K. T. Dolder, *Measurements of inelastic collisions between homonuclear ions: Na^+, K^+ and Rb^+* , J. Phys. B, V.14, p.L603 (1981).
- [21] G. C. Angel and K. F. Dunn and P. A. Neill and H. B. Gilbody, *Charge transfer and ionisation in $Xe^+ - Xe^+$ collisions*, J. Phys. B, V.13, p.L391 (1980).
- [22] K. F. Dunn and G. C. Angel and H. B. Gilbody, *An experimental study of charge transfer and ionisation in $Cs^+ - Cs^+$ collisions*, J. Phys. B, V.12, p.L623 (1979).

- [23] B. Peart and R. A. Forrest and K. T. Dolder, *Measurements of inelastic collisions between Cs^+ ions*, J. Phys. B, V.14, p.1655 (1981).
- [24] P. A. Neill and G. C. Angel and K. F. Dunn and H. B. Gilbody, *Collisions between Cs^+ ions—a further experimental study*, J. Phys. B, V.15, p.4219 (1982).
- [25] B. K. Stalder and K. H. Berkner and R. V. Pyle, Phys. Rev. A, V.29, p.3052 (1984).
- [26] R. A. Forrest and B. Peart and K. T. Dolder, *Measurements of inelastic collisions between Tl^+ ions*, J. Phys. B, V.15, p.L45 (1982).
- [27] H. J. Kim and R. K. Janev, *Electron-loss cross sections in symmetric multicharged-ion collisions*, Phys. Rev. Lett., V.58, p.1837 (1987).
- [28] S. Meuser and F. Melchert and S. Krudener and A. Pfeiffer and K. von Diemar and E. Salzborn, *Crossed-beams arrangement for the investigation of charge-changing collisions between multiply charged ions*, Rev. Sci. Instrum, V.67, p.2752 (1996).
- [29] F. Melchert, private communication (1997).
- [30] A. Pfeiffer and S. Krudener and F. Melchert and L. P. Presnyakov and R. Schulze and S. Meuser and T. Bartsch and C. Brandau and K. v. Diemar and K. Huber and E. Salzborn, *Angular differential cross section measurements in light ion-ion collision systems*, Nucl. Instr. and Meth., V.B98, p.240 (1995).

- [31] S. Krudener and F. Melchert and K. v. Diemar and A. Pfeiffer and K. Huber and E. Salzborn, *Observation of interference in charge exchange scattering in $He^{2+} + He^+$ collisions*, Phys. Rev. Lett., V.79, p.1002 (1997).
- [32] W. Fritsch, in *Review of Fundamental Processes and Applications of Atoms and Ions*, edited by C. D. Lin, published by World Scientific, p.253-256 (1993).
- [33] Thomas G. Winter, *Electron transfer in $p-He^+$ and $He^{2+}-H$ collisions using a Sturmian basis*, Phys. Rev. A, V.25, p.697 (1982).
- [34] Thomas G. Winter, *Triple-center treatment of electron transfer and ionization in $He^{2+}-H$ and $p-He^+$ collisions*, Phys. Rev. A, V.37, p.4656 (1988).
- [35] B. H. Bransden and C. J. Noble and J. Chandler, *Theoretical studies of the interaction of He^{2+} with $H(1s)$ and H^+ with He^+* , J. Phys. B, V.16, p.4191 (1983).
- [36] W. Fritsch and C. D. Lin, *Close-coupling calculations for inelastic processes in intermediate energy ion-atom collisions*, J. Phys. B: At. Mol. Phys., V.15, p.1255 (1982).
- [37] M. Kimura, *Single- and double-electron capture in $He^{2+} + He$ collisions and single-electron capture in $He^+ + He^+$ collisions*, J.Phys. B, V.21, p.L19 (1988).
- [38] W. Fritsch and C. D. Lin, *Two-electron description of electron transfer in $He^+ + He^+$ collisions*, Phys. Lett. A, V.123, p.128 (1987).

- [39] K. Gramlich and N. Grun and W. Scheid, *coupled-channel calculations with Gauss-type orbitals for charge transfer and ionisation in collisions of the $(He - He)^{2+}$ system*, J. Phys. B, V.22, p.2567 (1989).
- [40] S. L. Willis and G. Peach and M. R. C. McDowell and J. Banerji, *Charge transfer and ionisation processes in collisions involving atoms and ions of hydrogen and helium*, J. Phys. B, V.18, p.3939 (1985).
- [41] F. Melchert and M. Benner and S. krudener and R. Schulze and S Meuser and K. Huber and E. Salzborn, *Neutralization of H^- in energetic collisions with multiply charged ions*, Phys. Rev. Lett., V.74, p.888 (1995).
- [42] D. R. Bates and Anne H. Boyd, *Effect on symmetrical resonance charge transfer cross sections of change in relative motion during encounter*, Phys. Soc., V.80, p.1301 (1962).
- [43] A. S. Dickinson and D. W. Hardie, *Symmetric resonance charge transfer in $He^+(1s)-He^{2+}$ collisions*, J. Phys. B, V.12, p.4147 (1979).
- [44] C. A. Falcon, *Charge exchange in low-energy ${}^3He^+ - {}^4He^{2+}$ collisions*, J. Phys. B, V.16, p.1793 (1983).
- [45] C. Forster and R. Shingal and D. R. Flower and B. H. Bransden and A. S. Dickinson, *Total and differential cross sections for charge exchange in $He^{2+}-He^+$ collisions: trajectory effects*, J. Phys. B, V.21, p.3941 (1988).

- [46] J. N. Bardsley and P. Gangopadhyay and B. M. Penetrante, *Symmetric charge transfer to multiply charged ions*, Phys. Rev. A, V.40, p.2742 (1989).
- [47] A. Jognaux and F. Brouillard and S. Szucs, *Charge exchange in low energy $He^+ - He^{2+}$ collisions*, J. Phys. B, V.11, p.L669 (1978).
- [48] B. Peart and K. Dolder, *Measurements of cross sections for charge exchange between $^4He^+$ and $^3He^{2+}$ ions*, J.Phys. B, V.12, p.4155 (1979).
- [49] F. Melchert, K. Huber, S. Krudener, R. Schulze, S. Meuser, S. Pfaff, S. Petri, M. Benner and E. Salzborn, *Resonant charge transfer in $He^{2+} + He^+$ collisions*, AIP conference proceedings NO. 274, p.493 (1992).
- [50] F. Melchert and S. Krudener and R. Schulze and S. Petri and S. Pfaff and E. Salzborn, *Measurements of resonant charge transfer in $He^{2+} - He^+$ collisions*, J.Phys. B, V.28, p.L355 (1995).
- [51] R. K. Janev and D. S. Belic, *Quasi-resonant charge exchange collisions between multiply charged ions.*, J.Phys. B, V.15, p.3479 (1982).
- [52] R. K. Janev and D. S. Belic, *Double resonant charge exchange in ion-ion collisions*, Phys. Lett., V.89A, p.190 (1982).
- [53] Thomas G. Winter, *Electron transfer and ionization in collisions between protons and the ions $He^+, Li^{2+}, Be^{3+}, B^{4+}$, and C^{5+} studied with the use of a Sturmian basis.*, Phys. Rev. A, V.35, p.3799 (1987).

- [54] C. Brandau and F. Melchert and S. Krudener and S. Meuser and A. Pfeiffer and K. V. Diemar and T. Bartsch and E. Salzborn and D. B. Uskov and A. D. Ulantsev and L. P. Presnyako, *Quasi-resonant charge exchange between carbon and boron ions*, J. Phys. B, V.28, p.L579 (1995).
- [55] C. Brandau and S. Krudener and F. Melchert and L. P. Presnyakov and R. Schulze and S. Meuser and T. Bartsch and K. V. Diemar and A. Pfeiffer and K. Huber and E. Salzborn, *Quasi-resonant charge exchange in $C^{2+} + B^+$ collisions.*, Nucl. Instr. and Meth., V.B98, p.243 (1995).
- [56] F. Brouillard, in *Physics of electron-ion and ion-ion collisions*, edited by F. Brouillard and J. W. McGowan, published by Plenum/New York, p.415 (1983).
- [57] M. Liehr *et al*, International Conference on ECR Ion Sources and their Applications, NSCL Report MSUCP-47 (1987).
- [58] R. W. McCullough *et al*, Proceedings of the 11th Intern. Workshop on ECRIS, KVI-Report 969, p.195 (1993).
- [59] V. Needham, DualScan pc program.
- [60] XSYS/IUCF VME Data Acquisition Software, Indiana University Cyclotron Facility, Bloomington, IN 47405.
- [61] F. Brouillard and J. M. Delfosse, *A Method of Measuring Ion-Ion Exchange Cross Sections Using Coincidence Technique*, in *Proc. 5th Int. Conf. on Physics*

- of *Electronic and Atomic Collisions*, published by North-Holland Publishing Co., p.159 (1967).
- [62] E. Y. Kamber and A. G. Brenton and S. Hughes, *State-Selective single-electron stripping processes of Ar^{2+} ions in collisions with He and Ar*, J. Phys. B, V.23, p.L311 (1990).
- [63] E. Sidky, I. Reiser and C. D. Lin, private communication (1997).
- [64] D. A. Church, *Collision measurements and excited-level lifetime measurements*, Phys. Reports., 228 253, p.315 (1993).
- [65] J. B. Hasted, in *Advances in atomic and molecular physics*, edited by D. R. Bates and B. Bederson, V.15, p.206-211 (1979).
- [66] J. B. Hasted and M. A., D. Phil., *Physics of atomic collisions*, published by American Elsevier, p.612-621 (1972).
- [67] SIMION for the PC is developed by Idaho National Engineering Laboratory, Chemical Materials & Processes Department, Lockheed Idaho Technologies Company, Idaho Falls, ID 83415.
- [68] C. Lewis Cocke, *Beam-Foil Spectroscopy*, in *Methods of experimental physics*, edited by D. Williams, published by Academic Press, Inc., V.13, part B, p.256-259 (1976).

- [69] D. W. Savin and L. D. Gardner and D. B. Reisenfeld and A. R. Young and J. L. Kohl, *In situ absolute calibration of a channel electron multiplier for detection of positive ions*, Rev. Sci. Instrum., V.66, p.67 (1995).
- [70] S. Winecki, Master thesis, Kansas State University, p.315 (1995).
- [71] P. R. Bevington and D. Keith Robinson, *Data reduction and error analysis for the physical sciences*, published by McGraw-Hill, Inc., chap.3 (1992).